Czech Technical University in Prague
Faculty of Nuclear Sciences and Physical Engineering
Department of Physics

Programme: Mathematical Engineering
Branch of Study: Mathematical Physics

High p_T jets in RunII of the ATLAS Experiment

MASTER'S DEGREE PROJECT

Author: Jan Lochman
Supervisor: Ing. Zdeněk Hubáček, Ph.D.
Submitted in: May 2015

Zadani prace

Statement

Prohlasuji. . .

V Praze dne ....

Jan Lochman

Acknowledgment

Dekuji...

Jan Lochman

Název práce:

Jety s vysokou příčnou hybností v RunII experimentu ATLAS

Autor: Jan Lochman

Obor: Matematické Inženýrství

Druh práce: Diplomová práce

Vedoucí práce: Ing. Zdeněk Hubáček, Ph.D.
CERN

Abstrakt: Abstrakt CZ

Klíčová slova: Klicova slova

Title:

High p_T jets in RunII of the ATLAS Experiment

Author: Jan Lochman

Abstract: This thesis deals with the meassurement of the inclusive jet double differential cross section in p_T and rapidity using PYTHIA8 generated events of pp colisions at $\sqrt{s} = 13\,\mathrm{TeV}$ with the ATLAS detector response reconstructed by GEANT4 detector simulation. Differential cross section obtained from the detector level is unfolded on the particle level and compared with the parton level cross section prediction of the NLO pQCD. Two different approaches of unfolding denoted as the simple and 2D unfolding are used and results of these two approaches are compared. Both PYTHIA8 and NLO pQCD have used CT10 PDFs and ATLAS underlying event tune AU2.

Key words: Quantum Chromodynamics, Jets, Unfolding

Contents

List of Tables

List of Figures

Introduction

Search for the superior equation which would be able to explain all about the physical universe we do observe, sometimes called the Theory of Everything, led some of the physicists to the concept of elementary particles some of which define the building blocks of our observable universe whereas the remaining govern the way how they interact.

From the beginning of the twentieth century, the term of elementary particle was redefined with new generation of physicists as is illustrated in Figure 1. The latest reform was caused by quarks and the invention of Quantum Chromodynamics describing its strong interaction which is next to the electromagnetic and weak interactions encapsulated by the present theory of elementary particles called the Standard Model.

Although the Standard Model contains mechanism for assigning elementary particles masses, gravity was not included in the Standard Model up to date because the present attempts of quantization of gravity and description of the gravitation as the interaction mediated by the quanta of gravity, known as gravitons, led to unrenormalizable theories. There are others by the Standard Model unresolved questions including the nature of the dark part of our universe and the origin of the matter-antimatter asymmetry.

We know that the Standard Model is not the ultimate Theory of Everything, but it successfully stands against present results from particle physics experiments. Last discoveries of elementary particles occured on $\sim 100\,\mathrm{GeV}$ energy scale with top quark discovery [12,13] with mass $173.34 \pm 0.98\,\mathrm{GeV}$ in 1995 at Tevatron and Higgs boson discovery [14] with mass $125.09 \pm 0.32\,\mathrm{GeV}$ in 2012 at CERN and both were successfully predicted by the Standard Model. If there is new physics beyond the Standard Model on $\sim$ TeV scale, the LHC Run II could be the first to discover it [15].

This thesis deals with the measurement of the double differential inclusive jets cross section in p_T and rapidity. Jets are the dominant objects observed by inelastic collisions on hadron colliders dominating any other observable physics process in orders of magnitude and covering wide range of momentum transfers. Inclusive jets measurements may therefore serve as the test for both ATLAS detector performance as well as may be able to reveal some discrepancy in the Standard Model predictions.

First Chapter of this thesis deals with the Quantum Chromodynamics

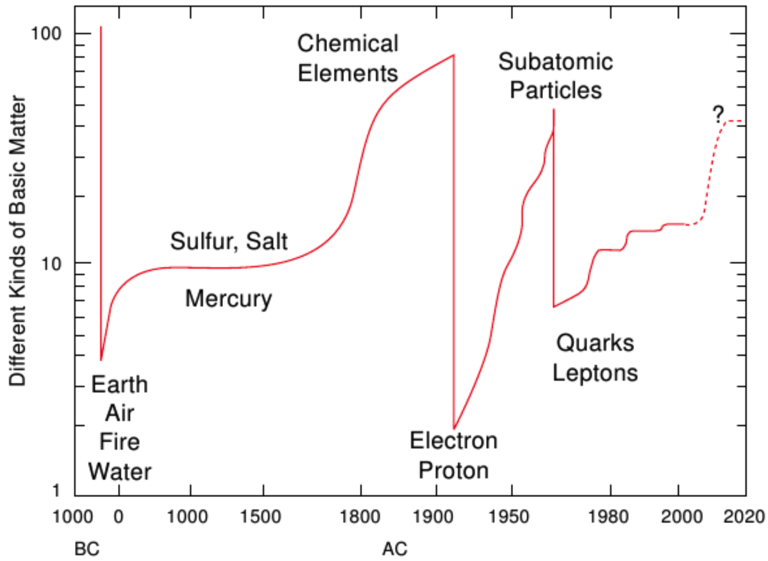

Figure 1: History of elementary particle physics. Figure From [1].

and follows the historical development including the experiments which led to the removal of the proton from the list of elementary particles and replacing it by the quarks. QCD will be formulated as a quantum field theory and the phenomenon known as the running coupling constant will be discussed in order to divide the QCD into perturbative and non-perturbative regions.

In the second Chapter, the Large Hadron Collider will be presented with detailed description of the ATLAS detector. The basic features of QCD introduced in the previous chapter will be used to define jets - objects we do dominantly observe by inelastic collisions on hadron colliders. The jet reconstruction on ATLAS detector including description of jet calibration and unfolding of observed spectra will be presented in this chapter as well.

Third chapter describes the steps of the inclusive jets analysis beginning with the characteristics of Monte Carlo data used, including event selection criteria. Two approaches of unfolding are used to unfold p_T spectra on detector level to particle level. Results obtained from both approaches are compared with each other and with the next-to-leading order perturbative QCD prediction on parton level.

Chapter 1

QCD

Is the purpose of theoretical physics to be no more than a cataloging of all the things that can happen when particles interact with each other and separate? Or is it to be an understanding at a deeper level in which there are things that are not directly observable (as the underlying quantized fields are) but in terms of which we shall have a more fundamental understanding?

Julian Schwinger

The theoretical framework of particle physics is called the Standard Model (SM). The SM describes the way how the fundamental components of matter interact with each other through strong, weak and electromagnetic interactions. Mathematically the SM is a gauge quantum field theory with local internal symmetries of the direct product group $SU(3) \times SU(2) \times U(1)$. Gauge bosons are assigned to generators of this symmetry - there are 8 massless gluons from $SU(3)$ and 3 massive $W^{\pm}, Z$ bosons with 1 massless boson γ from electroweak $SU(2) \times U(1)$ sector. Higgs mechanism has to be introduced in the electroweak sector to assign $W^{\pm}, Z$ bosons masses and as consequence the new particle - Higgs boson - emerges in the SM theory. All bosons have integer spin.

In addition to the bosons the SM introduces spin-1/2 fermions which are divided into three quark and three lepton families. Fermions are assumed to be point-like because there is no evidence for their internal structure to date. All fermions interact weakly, if they have electrical charge, they interact electromagnetically as well. Quarks are the only fundamental fermions which do interact strongly. System of fundamental particles of the SM is shown in Figure 1.1.

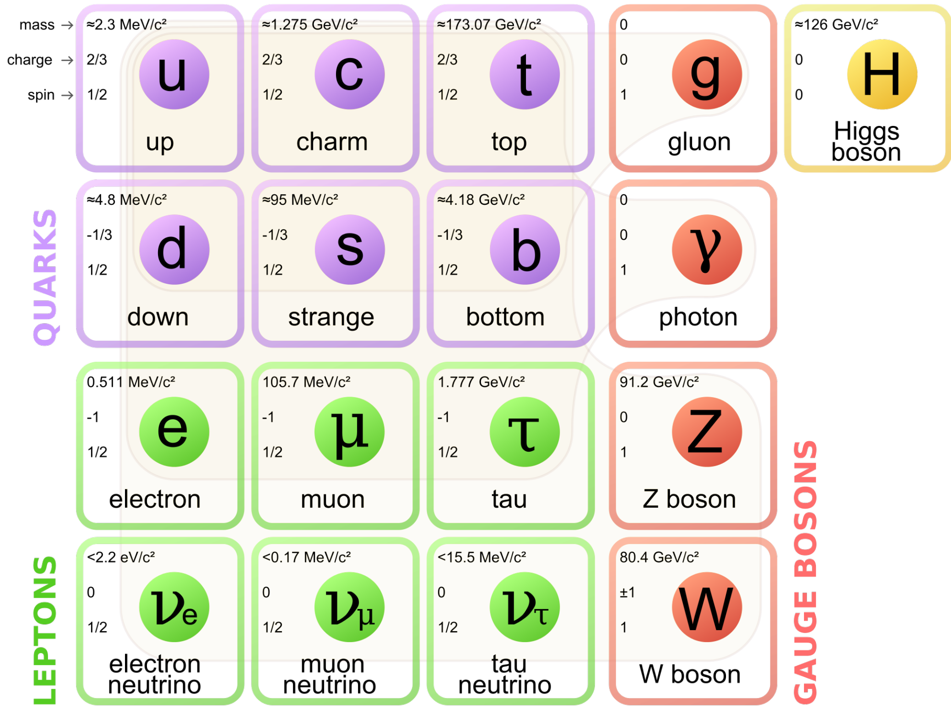

Figure 1.1: The system of fundamental particles of the SM. Figure from [2].

Quarks bind together to form hadrons and there are hundreds [16] of known hadrons up to date. Hadrons are divided into baryons (3 quarks) and mesons (quark and anti-quark pairs). Theory describing the interaction between quarks is called Quantum Chromodynamics (QCD) which key features will be discussed in this chapter. The reasoning for quark existence and for the description their strong interaction as $SU(3)$ gauge theory will be presented. Running coupling constant will be discussed to split QCD into perturbative and non-perturbative regions - two regions, where QCD has to use different mathematical approaches for the description of strong interaction. Most of ideas presented here is overtaken from the following textbook [5]. Electroweak sector of the SM is described in [17]. For more concise information about the SM the following textbooks can serve [18, 19].

1.1 Theoretical Ansatz

In 1950s, there have already been discovered tens of new hadrons thanks to new particle accelerators and a lot of effort was exerted to categorize them. To each particle there was assigned a series of quantum numbers including isospin T with its third component T_3, hypercharge Y, electrical charge Q, strangeness S, baryon number B and others. Soon it was recognized, that

	S	Y	T	T_3	Q
p	0	1	1/2	1/2	1
n				-1/2	0
Σ^+	-1	0	1	1	1
Σ^0				0	0
Σ^-				-1	-1
Λ			0	0	0
Ξ^0	-2	-1	1/2	1/2	0
Ξ^-				-1/2	-1

Table 1.1: Quantum numbers of selected baryons known in 1950s. S strangeness, Y hypercharge, T isospin, T_3 third component of isospin, Q electrical charge.

there are some symmetries between these quantum numbers, like famous Gell-Mann–Nishijima relation [20, 21]

$$Q = T_3 + 1/2Y \quad , \quad Y = B + S + \dots, \tag{1.1}$$

where dots denote charm, bottomness and topness and were introduced after work of Gell-Mann and Nishijima. Some of the baryons known by then are shown in Table 1.1. In 1960s, the known hadrons were successfully categorized with the so called Eightfold Way, which was published independently by Murray Gell-Mann [22] and George Zweig [23] in 1964. The Eightfold Way successfully predicted the existence of new particle Ω^- including its mass. Basic ideas of Eightfold Way will be discussed in this section.

The key feature of Eightfold Way is to understand hadrons as the part of different representations of infinitesimal generators of $SU(3)$ flavor symmetry group. These infinitesimal generators of $SU(3)$ form the real eight-dimensional Lie algebra $\mathfrak{su}(3)$ which fundamental representation is usually derived from Gell-Mann matrices

$$\begin{aligned}
&\lambda_1 = \begin{pmatrix} 0 & 1 & 0 \\ 1 & 0 & 0 \\ 0 & 0 & 0 \end{pmatrix} \quad \lambda_2 = \begin{pmatrix} 0 & -i & 0 \\ i & 0 & 0 \\ 0 & 0 & 0 \end{pmatrix} \quad \lambda_3 = \begin{pmatrix} 1 & 0 & 0 \\ 0 & -1 & 0 \\ 0 & 0 & 0 \end{pmatrix} \\
&\lambda_4 = \begin{pmatrix} 0 & 0 & 1 \\ 0 & 0 & 0 \\ 1 & 0 & 0 \end{pmatrix} \quad \lambda_5 = \begin{pmatrix} 0 & 0 & -i \\ 0 & 0 & 0 \\ i & 0 & 0 \end{pmatrix} \\
&\lambda_6 = \begin{pmatrix} 0 & 0 & 0 \\ 0 & 0 & 1 \\ 0 & 1 & 0 \end{pmatrix} \quad \lambda_7 = \begin{pmatrix} 0 & 0 & 0 \\ 0 & 0 & -i \\ 0 & i & 0 \end{pmatrix} \quad \lambda_8 = \frac{1}{\sqrt{3}} \begin{pmatrix} 1 & 0 & 0 \\ 0 & 1 & 0 \\ 0 & 0 & -2 \end{pmatrix}.
\end{aligned} \tag{1.2}$$

The generators are usually chosen $g_a = \frac{1}{2}\lambda_a$ and obey the commutation

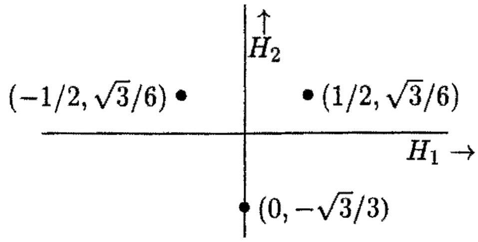

Figure 1.2: Eigenvalues of 3-dimensional representation of $\mathfrak{su}(3)$ Lie algebra. Figure from [3].

relation $[g_a, g_b] = i f_{abc} g_c$ with f_{abc} being structure constants. Cartan subalgebra of fundamental representation of $\mathfrak{su}(3)$ is generated by $H_1 = g_3$ and $H_2 = g_8$. The eigenstates of three-dimensional representation of $\mathfrak{su}(3)$ can be chosen

$$u = \begin{pmatrix}1\\0\\0\end{pmatrix} \leftrightarrow \left(\frac{1}{2}, \frac{\sqrt{3}}{6}\right), \quad d = \begin{pmatrix}0\\1\\0\end{pmatrix} \leftrightarrow \left(-\frac{1}{2}, \frac{\sqrt{3}}{6}\right), \quad s = \begin{pmatrix}0\\0\\1\end{pmatrix} \leftrightarrow \left(0, -\frac{\sqrt{3}}{3}\right), \tag{1.3}$$

where the eigenvalues to generators of the Cartan subalgebra was assigned $H_1 u = \frac{1}{2} u$, $H_2 u = \frac{\sqrt{3}}{6} u$ and similarly for d and s eigenstates. These eigenvalues are shown in Figure 1.2. Other important representation of $\mathfrak{su}(3)$ is eight-dimensional adjoint representation. This representation has the following eigenstates and corresponding eigenvalues

$$\begin{aligned}
&\frac{1}{\sqrt{2}}(g_1 \pm i g_2) \leftrightarrow (\pm 1, 0), \\
&\frac{1}{\sqrt{2}}(g_4 \pm i g_5) \leftrightarrow \left(\pm\frac{1}{2}, \pm\frac{\sqrt{3}}{2}\right), \\
&\frac{1}{\sqrt{2}}(g_6 \pm i g_7) \leftrightarrow \left(\mp\frac{1}{2}, \pm\frac{\sqrt{3}}{2}\right),
\end{aligned} \tag{1.4}$$

where again when denoting $A = \frac{1}{\sqrt{2}}(g_1 + i g_2)$ then the upper sign of the first expression reads $[H_1, A] = A$ and $[H_2, A] = 0$ and similarly for remaining 5 eigenstates. Defining

$$H_1 = T_3 \quad \text{and} \quad H_2 = \frac{\sqrt{3}}{2} Y \tag{1.5}$$

one can easily assign hadrons from table 1.1 to corresponding eigenvalues of adjoint representation in (1.4) according to its third component of isospin T_3 and its hypercharge Y. This is depicted in Figure 1.3.

When the same redefinition is done to the eigenstates of three-dimensional representation in (1.3), one can assign to eigenstates the hypercharge Y and

	S	Y	T	T_3	Q
u	0	1/3	1/2	1/2	2/3
d				-1/2	-1/3
s	-1	-2/3	0	0	

Table 1.2: Quantum numbers of three quarks which existence was predicted by Gell-Mann and Zweig in 1964.

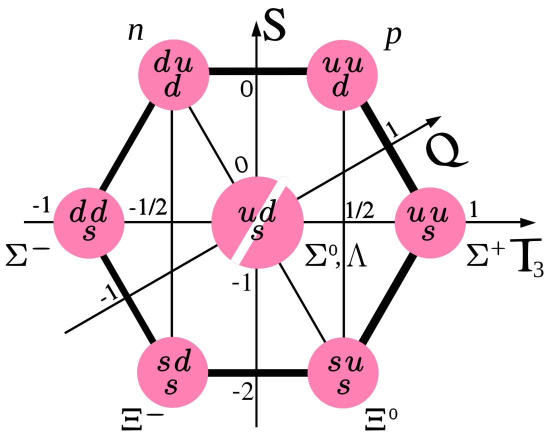

Figure 1.3: Baryonic octuplet encapsulating baryons from table 1.1. For baryons in this diagram, the relation $Y = S + 1$ holds. Figure from [4].

strangeness S as well. The concrete values for states u, d, s are shown in Table 1.2.

It is possible to find another representations of Lie algebra, to which the observed hadrons can be assigned. The simplest way seems to be through highest weight defining representation. From eigenvalues of adjoint representation (1.4) one can find simple roots $\alpha^1 = \left(\frac{1}{2}, \frac{\sqrt{3}}{2}\right)$, $\alpha^2 = \left(\frac{1}{2}, -\frac{\sqrt{3}}{2}\right)$, from which the highest weights follow $\mu^1 = \left(\frac{1}{2}, \frac{\sqrt{3}}{6}\right)$, $\mu^2 = \left(\frac{1}{2}, -\frac{\sqrt{3}}{6}\right)$. New representation of Lie algebra can be constructed from highest weight. This procedure is described in [3] in detail.

Representations defined by highest weight μ^1 or μ^2 respectively are called fundamental. Fundamental representation defined by μ^1 is usually denoted $\mathbf{3}$ and was encountered already by expressions (1.3) with weight diagram at Figure 1.2, corresponding to three different quark states. The second fundamental representation corresponds to three anti-quark states and is usually denoted $\bar{\mathbf{3}}$. Representation depicted in Figure 1.3 is defined by the highest weight $\mu^1 + \mu^2$.

Special interest is in representations with dimensions 10 and 8. These are present in decompositions $\mathbf{3} \otimes \mathbf{3} \otimes \mathbf{3} = \mathbf{10} \oplus \mathbf{8} \oplus \mathbf{8} \oplus \mathbf{1}$, which correspond to the baryons composed of three quarks, and $\mathbf{3} \otimes \bar{\mathbf{3}} = \mathbf{8} \oplus \mathbf{1}$ corresponding to mesons from quark and anti-quark.

Important feature of quark model just presented is its capability to predict hadron masses. This is done using Gell-Mann–Okubo mass formula [24, 25]

$$M = a_0 + a_1 S + a_2 \left(T(T+1) - \frac{1}{4} S^2 \right), \tag{1.6}$$

where a_0, a_1 and a_2 are free parameters which are common for all hadrons in one multiplet.

In 1970 Sheldon Lee Glashow, John Iliopoulos and Luciano Maiani proposed [26] an extension which predicted existence of fourth flavor of quark - charm quark. In 1973 the Makoto Kobayashi and Toshihide Moskawa proposed [27] that the existence of 6 different quark flavors could explain the experimental observation of CP violation.

1.2 Experimental Ground

In the previous section it was shown the hadrons can be categorized using representations of $\mathfrak{su}(3)$ Lie algebra. This lead to the model, where baryons were composed of three quarks whereas the mesons of quark and anti-quark. In this section, some experimental evidences will be presented to support quark model. First the scattering reactions will be discussed. It will be shown, that the lepton scattering on nucleons can be explained by assumption, that nucleons are composed of point-like spin-1/2 particles. Next discussion will address the fact, that there are three color charges - this will encounter the question, why the group $SU(3)$ is connected to the theory of strong interaction.

1.2.1 Scattering Reactions

One of the possibilities, how to find out, if there is some inner structure in nucleon N, are the scattering reactions

$$e^- \, (E \gg 1\,\text{GeV}) + N \to e^- + N, \tag{1.7}$$
$$\nu_e \, (E \gg 1\,\text{GeV}) + N \to \nu_e + N, \tag{1.8}$$

where the condition $E \gg 1\,\text{GeV}$ is explicitly written to ensure the wavelength of lepton being $< 0.2\,\text{fm}$. By the first scattering reaction, the information about electric charge distribution in nucleon can be extracted, whereas the second scattering reaction informs us about weak charge distribution. Further only (1.7) will be discussed. Feynmann diagram of this process is depicted with kinematics variables and vertex algebraic structures in Figure 1.4.

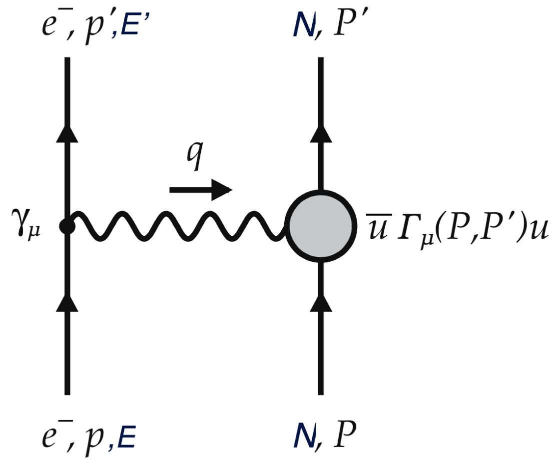

Figure 1.4: Scattering reaction $e^-N \to e^-N$ with kinematics variables and algebraic structures of vertices. Figure from [5].

Because of Lorentz-invariance of Quantum Electrodynamics (QED), the matrix element of the nucleon vertex $\bar{u}(P', S')\Gamma_\mu u(P, S)$ has to be a Lorentz-vector. This restricts the possible form of Γ_μ to the following algebraic structure

$$\Gamma_\mu = A\gamma_\mu + BP'_\mu + CP_\mu + iDP'^\nu\sigma_{\mu\nu} + iEP^\nu\sigma_{\mu\nu}, \tag{1.9}$$

where $A,\ldots,E$ depend only on Lorentz-invariant quantities. Next condition which has to be taken into account, is gauge invariance of matrix element, which can be written in the form

$$q^\mu\bar{u}(P', S')\Gamma_\mu u(P, S). \tag{1.10}$$

The further computation of cross section is straightforward and the result can be easily generalized to non-elastic scattering by which the nucleon in final state decays. The result is usually written using inelasticity parameter $y = \frac{E-E'}{E}$, $0 \le y \le 1$, $y = 0$ corresponding to the elastic scattering, Bjorken variable $x = \frac{Q^2}{2P\cdot q}$, $0 < x \le 1$, $x = 1$ denoting elastic scattering and finally instead of negative value q^2 the $Q^2 = -q^2$ is used. Final result can be than written in the form

$$\left.\frac{d^2\sigma}{dxdy}\right|_{eN} = \frac{8\pi M_N E\alpha^2}{Q^4}\left[xy^2F_1^{eN}(Q^2, x) + (1-y)F_2^{eN}(Q^2, x)\right]. \tag{1.11}$$

The eN sub(super)script stresses the fact, we are dealing with scattering (1.7). F_1^{eN} and F_2^{eN} are the so called structure functions, which are not determinable by the theory just presented - they have to be measured experimentally.

Structure constants were first measured by eP scattering at SLAC in 1968 [28] and shown the following results

1. for $Q^2 \geq 1\,\mathrm{GeV}$, there is no significant dependence of structure functions on Q^2 and
2. for $Q^2 \geq 1\,\mathrm{GeV}$, $F_2 \approx 2xF_1$.

These results can be explained by assumption nucleon being composed of point-like spin-1/2 constituents, for which R. P. Feynmann used the term partons. In the following basic ideas of parton model will be presented. To ith parton, it is possible to assign momentum $P_{i,\xi}$

$$P_{i,\mu} = \xi_i P_\mu + \Delta P_{i,\mu} \quad , \quad \max_\mu(\Delta P_\mu) \ll \max_\mu P_\mu, \tag{1.12}$$

where $\xi_i \in \langle 0, 1\rangle$ and $\Delta P_{i,\mu}$ comes from the interaction between partons and it is assumed, the momentum coming from this interaction is much smaller than the total nucleon momentum P_μ. In addition, probabilities $f_i(\xi_i)$ that ith parton will carry ξ_i fraction of total momentum fulfilling

$$\int d\xi_i f_i(\xi_i) = 1 \tag{1.13}$$

must be defined. Then for scattering reaction (1.7) the total cross section formula can be derived

$$\left.\frac{d^2\sigma}{dxdy}\right|_{eN} = \frac{4\pi M_N E\alpha^2}{Q^4}\left[y^2 + 2(1-y)\right]\sum_i f_i(x) q_i^2 x. \tag{1.14}$$

where for ith parton its electrical charge q_i was introduced. The last expression and (1.11) can be compared as polynomials in y resulting in

$$F_1^{eN}(x) = \frac{1}{2}\sum_i f_i(x) q_i^2 \quad , \quad F_2^{eN}(x) = \sum_i f_i(x) q_i^2 x. \tag{1.15}$$

It can be easily checked, that $F_2^{eN}(x) = 2xF_1^{eN}(x)$. Functions $f_i(x)$ just introduced are called Parton Distribution Functions (PDFs) and their important role in QCD will be discussed in 3.4 in more details.

Important conclusion from analyzing of scattering reactions is, that the experimental results can be explained by assumption nucleons being composed of spin-1/2 point-like partons, now called quarks.

1.2.2 Number of Colors

Despite the strong confidence in the parton model, a theory which would describe the interaction between partons was still missing. There was no direct evidence on how the theory would look like at the beginning of 1970s. The theory of electroweak unification successfully suggested, that the gauge theories are the right theories for the description of our world at the subatomic level, but to construct gauge theory of strong interaction the number of colors first had to be known.

Number of colors N_C is the number of different kinds of quarks of the same flavor with respect to the new interaction. In this part, three arguments will be presented to demonstrate, that $N_C = 3$.

The first argument is the analysis of the electron-positron annihilation into the pair of fermion and anti-fermion

$$e^+e^- \to f\bar{f}. \tag{1.16}$$

Feynmann diagram of this reaction is shown in Figure 1.5a, where constants sitting in two vertices are emphasized. α stands for fine structure constants and Q_f for charge of fermion f in units of positron charge. Total cross section has to be proportional to

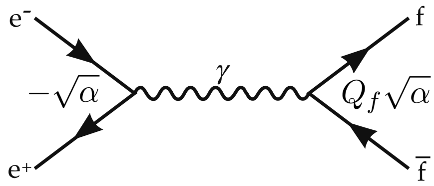

(a) $e^+e^- \to f\bar{f}$

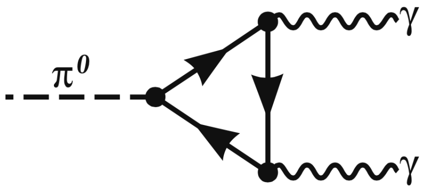

(b) $\pi^0 \to 2\gamma$

Figure 1.5: (a) e^-e^+ annihilation into the pair of fermion anti-fermion. Constants siting in both vertices are dented with α being the fine structure constant and Q_f the charge of fermion f in units of positron charge. (b) π^0 meson decay into pair of photons with closed fermion loop.

$$\sigma(e^-e^+ \to f\bar{f}) \sim Q_f^2\alpha^2. \tag{1.17}$$

In the case fermion f being quark, there is new degeneracy in final state coming from different colors of quarks in final state - the total cross section has to be multiplied by factor N_C. Experimentally, the so called R-factor is measured

$$R = \frac{\sigma(e^+e^- \to \text{hadrons})}{\sigma(e^+e^- \to \mu^+\mu^-)} = \left(\sum_q Q_q^2\right) N_C, \tag{1.18}$$

where the sum on the left hand side is over all possible quark states. When the quark model proposed by Gell-Mann a Zweig is used, then for the quark charges in Table 1.2

$$R = \left[\left(\frac{2}{3}\right)^2 + \left(\frac{-1}{3}\right)^2 + \left(\frac{-1}{3}\right)^2\right] N_C = \frac{2}{3}N_C. \tag{1.19}$$

Experimental results for R-ratio have shown [29], that $N_C = 3$.

The second argument is the measurement of decay width of π_0 meson. Decay is depicted in Figure 1.5b. For decay width Γ it can be derived

$$\Gamma = 7.63 \left(\frac{N_C}{3}\right)^2 \text{ eV}, \tag{1.20}$$

which, compared to the experimental value $\Gamma = 7.57 \pm 0.32\,\text{eV}$ [29], leads again to $N_C = 3$.

The third argument is purely theoretical and states, that the SM is internally consistent only if there are three colors [5]. This indicates that there is some linking between electroweak and strong sector of SM and motivates the search for Grand Unified Theories.

1.3 QCD as a Gauge Theory

Putting arguments of previous section all together, there is strong experimental evidence, that nucleons consist of point-like spin-1/2 particles called quarks and that quarks bring into the theory new degeneracy factor $N_C = 3$, which can be understood as three different strong charges called colors.

Nowadays the quark-quark strong interaction is understood as an $SU(3)$ gauge theory in a degree of freedom called color. Gell-Mann matrices (1.2) can be chosen as generators of $SU(3)$. These matrices act on quark color triplets wave functions

$$\psi(x) = \begin{pmatrix} \psi_r(x) \\ \psi_g(x) \\ \psi_b(x) \end{pmatrix}. \tag{1.21}$$

Following the Yang-Mills theory [30], to each generator $\frac{\lambda^a}{2}$ gluon field $A^a_\mu(x)$ and gluon field strength tensor

$$F^a_{\mu\nu} = \left(\partial_\mu A^a_\nu - \partial_\nu A^a_\mu + g f^{abc} A^b_\mu A^c_\nu\right) \tag{1.22}$$

is assigned where g denotes the coupling constant of strong interaction and f^{abc} are structure constant defined in section 1.1. QCD Lagrangian

$$\mathscr{L}_{\text{QCD}} = \bar{\psi}\left(-i\partial_\mu + g\frac{\lambda}{2}A^a_\mu(x)\right)\gamma^\mu\psi - \frac{1}{4}F^a_{\mu\nu}F^{\mu\nu}_a \tag{1.23}$$

is invariant under local transformation

$$\begin{aligned} \psi(x) &\to \psi'(x) = \mathrm{e}^{ig\Theta(x)}\psi(x), \qquad (1.24) \\ A_\mu(x) &\to \mathrm{e}^{ig\Theta(x)}\left(A_\mu(x) + \frac{i}{g}\partial_\mu\right)\mathrm{e}^{-ig\Theta(x)}, \end{aligned}$$

where

$$\Theta(x) = \frac{1}{2}\lambda^a\Theta^a(x) \quad , \quad A_\mu(x) = \frac{1}{2}\lambda^a A^a_\mu(x). \tag{1.25}$$

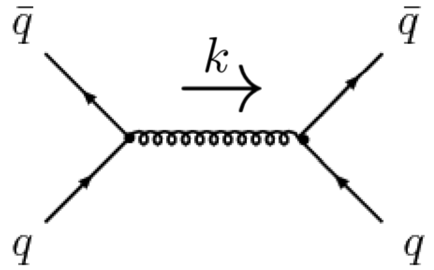

Figure 1.6: Leading order Feynmann diagrams in scattering reaction $q\bar{q} \to q\bar{q}$ with denoted transfered momentum k.

There is no mass term in Lagrangian (1.23) because mass term $m\bar{\psi}\psi$ vary under gauge transformation (1.24). Origin of mass term lies in Higgs mechanism [31] which is explained in [17] in details.

QCD Lagrangian (1.23) together with gauge transformations (1.24) are sufficient for determination of Feynman rules - key ingredient in perturbative QCD which will be discussed in next section.

By derivation of gluon propagator, one has to add to the QCD Lagrangain the so called gauge-fixing term

$$\mathscr{L}_{\text{QCD}}^{\text{gauge-fixing}} = -\frac{1}{2\xi} \left(\partial_\mu A_a^\mu\right)^2 , \tag{1.26}$$

which confines the possible gauges to one class parametrized by real parameter ξ. In non-Abelian gauge theories this term must be supplemented by the so called ghost term which brings into the theory new unphysical scalar particle obeying fermionic statistics. More details on so called Faddev-Popov ghost field can be found in [32].

1.4 Perturbative QCD

Quantum Electrodynamics (QED) and QCD are both quantum filed gauge theories, but they differ in one killing feature - the former is Abelian whereas the latter is not. The non-Abelian character of QCD leads to new phenomenons which have the origin in QCD Lagrangian (1.23) directly leading to triple and quartic gluonic interactions. In this section one remarkable consequence will be discussed - the running coupling constant.

Assume scattering process

$$q\bar{q} \to q\bar{q}, \tag{1.27}$$

which is depicted in the lowest order of perturbation theory by the Feynman graph in Figure 1.6. Except contribution of this graph to the scattering amplitude (which is the only contribution $\sim g^2$) there are 12 other Feynman diagrams with contributions $\sim g^4$. These are depicted in Figure 1.7.

The contributions from new Feynman diagrams are calculated in [5] in detail. There is shown, that all this contributions together are logarithmi-

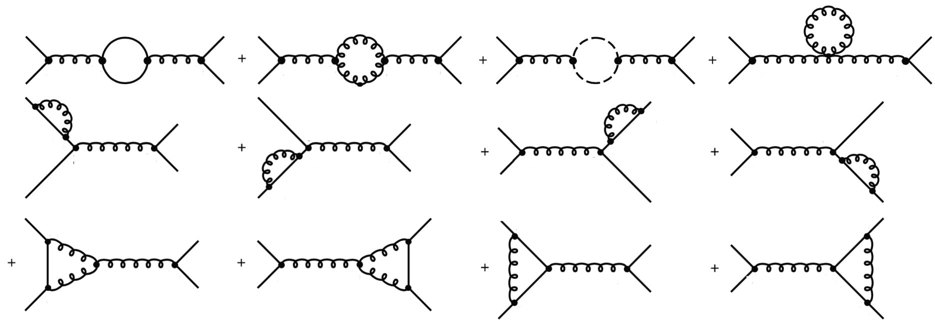

Figure 1.7: Next to the leading order Feynmann diagrams in scattering reaction $q\bar{q} \to q\bar{q}$. Dashed line represents scalar ghost particle.

cally divergent. This divergence can be removed, when from the scattering amplitude for arbitrary momentum transfer k^2 scattering amplitude for fixed momentum transfer $k^2 = -M^2$ is subtracted. This is how the renormalized coupling constant g_R is obtained and here is its final expression

$$g_R = g_0 - \frac{g_0^3}{16\pi^2}\left(\frac{11}{2} - \frac{1}{3}N_F\right)\ln\left(\frac{-k^2}{M^2}\right) + \mathscr{O}(g_0^5). \tag{1.28}$$

Here g_0 stands for the coupling constant measured at the renormalization scale $k^2 = -M^2$ and N_F is the number of different quark flavors with mass $m^2 \ll |k^2|$. Dependence of g_R on transfered momentum k^2 is evident, but there are another two intertwined dependences - on normalization scale M and on coupling constant at renormalization scale $g_0 = g_R|_{k^2=-M^2}$. For next purpose, it is convenient to use the dependence schema

$$g_R = g_R(-k^2, g_0(M)) \tag{1.29}$$

which allows the use of advantages of β-function and with the usage of the equation (1.28), the differential equation for $g_0(M)$ can be obtained

$$\beta(g_0) \equiv M\left(\frac{\partial g_R}{\partial M}\right)_{-k^2=M^2} = M\left(\frac{dg_0}{dM}\right)_{-k^2=M^2} \tag{1.30}$$

$$= -b_0 g_0^3 + \mathscr{O}(g_0^5), \quad b_0 = \frac{1}{16\pi^2}\left(11 - \frac{2N_F}{3}\right), \tag{1.31}$$

which can be solved directly to obtain coupling constant g_0 for arbitrary scale $-k^2$

$$\int_{g_0(M^2)}^{g_0(-k^2)} \frac{dg_0}{g_0^3} = -b_0 \int_{M^2}^{-k^2} \frac{dM}{M} \tag{1.32}$$

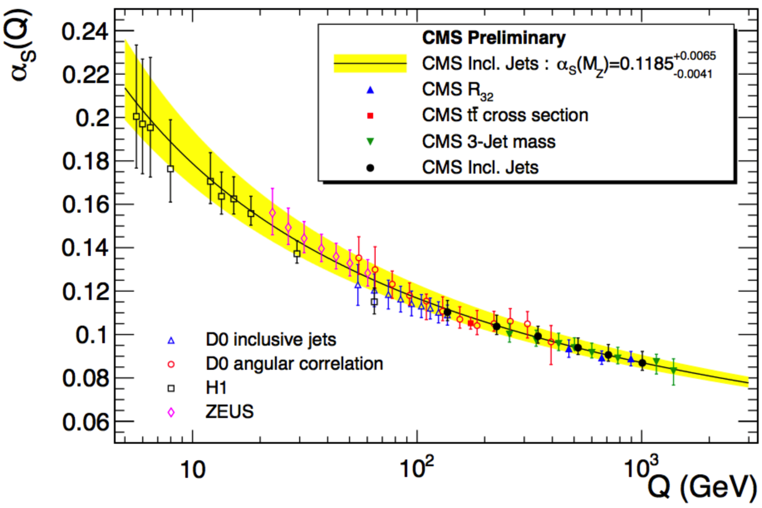

Figure 1.8: Experimental measurements of running coupling constant $\alpha_S(Q)$ (solid line) and its uncertainty (yellow band). $Q = \sqrt{|k^2|}$ in comparison to (1.33). Figure from [6].

with solution

$$\alpha_S(-k^2) = \frac{\alpha_S(M^2)}{1 + \frac{\alpha_S(M^2)}{4\pi}\left(11 - \frac{2N_F}{3}\right)\ln\left(\frac{-k^2}{M^2}\right)}, \quad g_0^2(-k^2) = 4\pi\alpha_S(-k^2), \tag{1.33}$$

which is the final expression for running coupling constant up to one-loop order. This dependence corresponds to experimental data which are depicted in Figure 1.8. Coupling constant decreases with increasing momentum transfer allowing the use of the perturbation theory. This is known as Asymptotic Freedom [33].

On the other hand, when the momentum transfer decreases, there is special value $-k^2 = \Lambda^2$ for which the last expression diverges

$$-1 = \frac{\alpha_S(M^2)}{4\pi}\left(11 - \frac{2N_F}{3}\right)\ln\left(\frac{\Lambda^2}{M^2}\right). \tag{1.34}$$

Experimental value is $\Lambda = 213^{+38}_{-35}\,\text{MeV}$ [34] and demonstrates, that perturbative QCD cannot be used at low energy transfers. In fact, the running coupling constant $\alpha_S(-k^2)$ reaches value ~ 1 on momenta transfers $\sqrt{|k^2|} \sim 500\,\text{MeV}$.

The behaviour of coupling constant at low energy transfers is not explainable in the language of perturpative QCD just presented. It is non-perturbative effect known as the principle of color confinment, which states, that quarks when seperate, the gluon force field between them becomes stronger and its energy is consumed by the creation of quark anti-quark pair. This continues until there is no free color charge left. This principle forbids us from observing free quarks.

To understand e.g. structure of proton with rest mass $< 1\,\mathrm{GeV}$ it is clear non-perturbative QCD has to be used. The ideas of non-perturbative QCD will be introduced in next section.

1.5 Non-Perturbative QCD

The most well established non-perturbative approach to QCD is the lattice QCD (LQCD). In this section basic features of the LQCD will be presented. More informations on this extended topic can be found in [5, 35].

LQCD is QCD formulated on a hypercubic equally spaced lattice in space and time with lattice parameter a denoting the distance between neighboring sites. Quark fields are placed on sites whereas the gluon fields sit on the links between neighboring sites. From QCD it inherits the gauge invariance which has to be formulated on lattice structure. For $a \to 0$ action of LQCD coincides with that of QCD. LQCD contains 6 parameters - strong coupling constant and masses of 5 quarks (the top quark with lifetime $\sim 10^{-24}\,\mathrm{s}$ is not assumed by the theory).

Unlike perturbative expansion used in continuous QCD, numerical evaluation of the path integral defining LQCD allows non-perturbative calculations. Practical LQCD calculations are limited by the availability of computational resources and the efficiency of algorithms. LQCD suffers with both statistical and systematic errors, the former arising from the use of Monte-Carlo integration, the latter, e.g. from the use of non-zero values of a.

Present LQCD calculations are made on supercomputers like the QCDCQ supercomputer [36] with peak speed of 500 TFlops using lattice spacing $a \sim 0.05 - 0.15\,\mathrm{fm}$ in lattice volume $V \sim (2 - 6\,\mathrm{fm})^3$.

The Importance of LQCD lies in its ability to predict mass spectrum of observed mesons and baryons, including quark masses itself, and in investigation of topological structure of QCD vacuum. LQCD can be used to obtain PDFs (1.13) helping us to understand the structure of hadrons. Phenomenology of LQCD explains also the principle of color confinment.

Chapter 2

Experimental Framework

What we observe is not nature itself, but nature exposed to our method of questioning.

Werner Heisenberg

In the previous chapter, the key features of QCD - today's theory of strong interaction - were introduced. The predictions of QCD are tested at particle accelerators persistently with no signs for new physics so far. Large Hadron Collider which will open energy regions not observed yet can change this very soon.

Jets are the most important objects observed by inelastic collisions on hadron colliders, which allows the QCD predictions to be confronted with the experiment. In this chapter, after the introduction of the Large Hadron Collider and the ATLAS detector, jet algorithms and the way how jets are reconstructed on the ATLAS detector will be described.

2.1 The Large Hadron Collider and The ATLAS Detector

2.1.1 The Large Hadron Collider

The Large Hadron Collider (LHC) [37,38] is a charged particle accelerator located on the border of France and Switzerland, near Geneva at CERN (the European Organization for Nuclear Research) in Switzerland. Built using the areas of the Large Electron-Positron collider, the main accelerator ring, of a 27 km circumference, is located around 100 m below the surface. There are four main experiments located around the ring: A Large Ion Collider Experiment (ALICE), A Toroidal LHC ApparatuS (ATLAS), Compact Muon

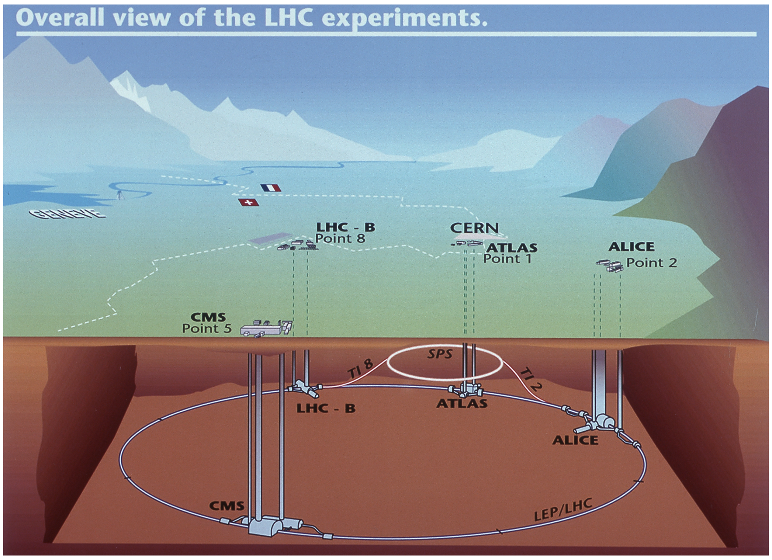

Figure 2.1: This diagram shows the locations of the four main experiments (ALICE, ATLAS, CMS and LHCb) that take place at the LHC. Located between 50 m and 150 m underground, huge caverns have been excavated to house the giant detectors. The Super Proton Synchotron (SPS), the final link in the pre-acceleration chain, and its connection tunnels to the LHC are also shown. Figure from [7].

Solenoid (CMS) and Large Hadron Collider beauty (LHCb). The complete accelerator and detector system is shown in Figure 2.1.

LHC started to operate on November 23, 2009 and soon thereafter (March 30, 2010) the proton-proton collisions achieved the center-of-mass energy $\sqrt{s} = 7\,\text{TeV}$, which is a half of the design energy of the machine. On April 5, 2012, the machine started its successful $\sqrt{s} = 8\,\text{TeV}$ run.

Next to the proton-proton collisions, first heavy-ion Pb-Pb collisions took place in 2010 at a center of mass energy per pair of colliding nucleons $\sqrt{s} = 2.76\,\text{TeV}$. Proton-Pb collisions at $\sqrt{s} = 5.02\,\text{TeV}$ occurring on LHC during 3 weeks of 2013 successfully demonstrated LHC capability to provide asymmetric collisions.

The first running period of the LHC, Run I, was very successful and resulted in the discovery of the Higgs boson on July 4, 2012 [14]. The accelerator complex including its experiments has been upgraded for two years and the Run II is expected to start in early summer 2015 [39, 40]. In Run II the center-of-mass energy of proton-proton collisions will be raised to $\sqrt{s} = 13\,\text{TeV}$ and the beam crossing time could be reduced from the current 50 ns to 25 ns. The expected integrated luminosity is expected to be $\sim 100\,\text{fb}^{-1}$ after three years of data collecting.

2.1.2 The ATLAS Detector

The ATLAS detector [41] is a general-purpose detector surrounding one of the interaction points of the LHC and with ~ 100 million of individual electronic channels it is the most complicated instrument ever created. The purpose of the ATLAS detector is to record particle collisions up to the center-of-mass energy per pair of colliding nucleons $\sqrt{s} = 14\,\mathrm{TeV}$. A detector overview is shown in Figure 2.2a, where the main sub-detector systems can be seen: the inner detector, used to reconstruct charged-particle tracks, the electromagnetic calorimeters, the hadronic calorimeters, and the muon spectrometer.

ATLAS uses a right-handed coordinate system with its origin at the interaction point in the center of the detector and the z axis along the beam pipe. The x axis points from the interaction point to the center of the LHC ring, and the y axis points upward. Cylindrical coordinates (r, ϕ) are used in the transverse plane, ϕ being the azimuthal angle around the beam pipe. Instead of polar angle θ, pseudorapidity η is often used. In this thesis the rapidity y is used as the polar angle coordinate. In following definitions of pseudorapidity η and rapidity y, E stands for the total energy and p for size of total momentum:

$$\eta = -\frac{1}{2}\ln\left(\frac{p+p_z}{p-p_z}\right) = -\ln\left[\tan\left(\frac{\theta}{2}\right)\right], \tag{2.1}$$

$$y = -\frac{1}{2}\ln\left(\frac{E+p_z}{E-p_z}\right). \tag{2.2}$$

The transverse momentum $p_T = \sqrt{p_x^2 + p_y^2}$ presents the component of momentum perpendicular to the beam line.

The main detector system relevant to this thesis is the ATLAS calorimeter, which is emphasized in Figure 2.2b. The calorimeter is divided into sub-detectors, providing overall coverage up to $|\eta| < 4.9$. The electromagnetic calorimeter, covering region $|\eta| < 3.2$, is a high-granularity sampling detector in which the liquid argon (LAr) active medium is interspaced with layers of lead absorber. The hadronic calorimeters are divided into three sections: a tile scintillator/steel calorimeter is used in both the barrel ($|\eta| < 1.0$) and extended barrel cylinders ($0.8 < |\eta| < 1.7$) while the hadronic endcap ($1.5 < |\eta| < 3.2$) consists of LAr/copper calorimeter modules. The forward calorimeter measures both electromagnetic and hadronic energy in the range $3.2 < |\eta| < 4.9$ using LAr/copper and LAr/tungsten modules.

2.2 Hadron Collision at LHC

In this section the phenomenological description of proton-proton collisions will be presented following Figure 2.3 and Reference about Monte Carlo event generators [29].

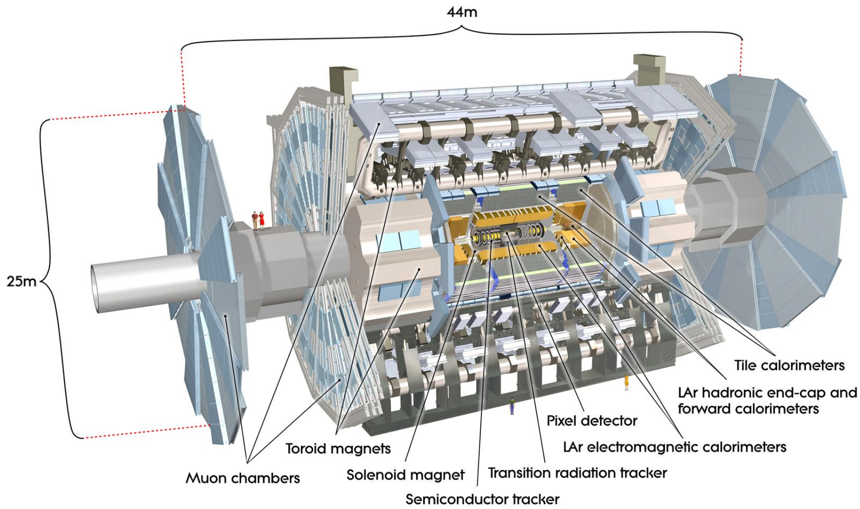

(a) ATLAS detector.

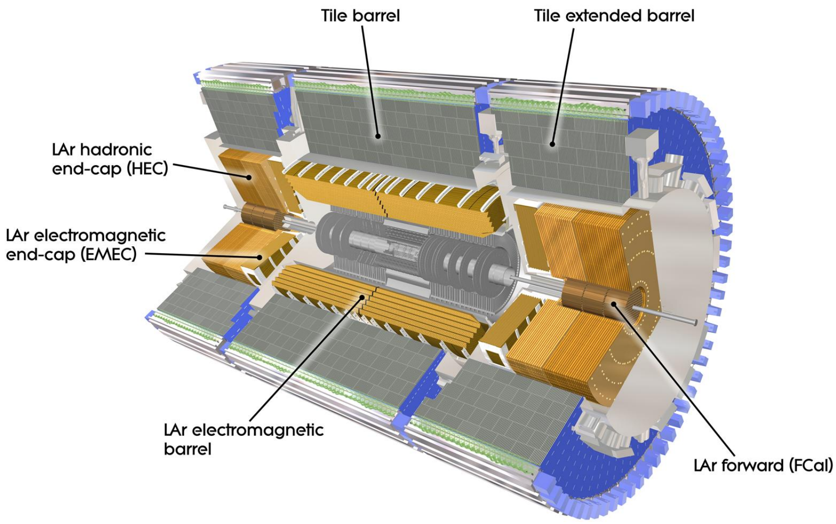

(b) Inner detector and calorimeter systems.

Figure 2.2: (a) an overview of the ATLAS detector (b) detail on the inner detector and the calorimeters - the dominant sub-detector systems used in this thesis. Figures taken from [8].

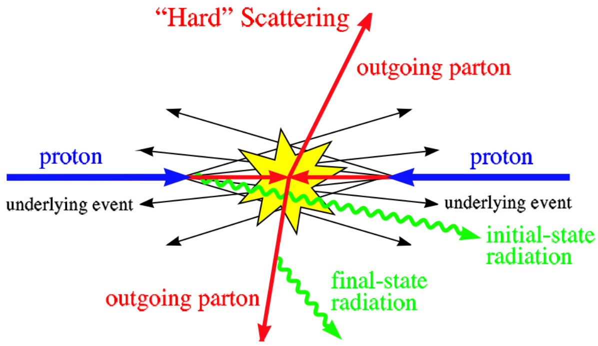

Figure 2.3: Schematic representation of a hard scattering proton-proton collision. Figure taken from [9].

Two incoming protons can be understood as two bags of partons. The collision is dominated by the strong interaction of two partons - one from each of the colliding hadrons. These partons are called incoming partons and the momentum transfer of their interaction is $Q \gg \Lambda$, so the perturbative QCD can be used to describe the process of hard scattering. The remaining energy is carried by the remaining partons, which create the so called underlying event - particles, which do not come from the hard QCD processes.

When partons are sufficiently far from each other, the non-perturbative QCD has to be used to describe the process of hadronisation, in which a set of colored partons is transformed into a set of colorless primary hadrons which may then decay further.

During the collision, the color charges of partons interact resulting in radiation of gluons $q \to qg$. This process is described by perturbative QCD and leads to infrared and collinear divergences. However, infrared divergences are canceled by Kinoshita–Lee–Nauenberg theorem [42, 43], so only collinear divergences remain. There is no mechanism known up to date, which would solve the problem with collinear divergences. However, observables inclusive enough to be insensitive to processes that distinguish between different numbers of partons are not affected by infrared divergences. There is no possibility how to theoretically predict the energy of hardest outgoing particle, but it is possible to predict the energy flow in a cone from the point of scattering.

This is where the term jet comes to play. A jet can be naively seen as a group of collimated particles generated by the hadronisation of a parton in the scattering process and is the most important object used on hadron colliders for analysis of QCD processes.

2.3 Jet Algorithms

Jet algorithm is a generic "recipe" which takes a set of particles (or other objects with defined four-momenta) and returns jets created from them. The jet algorithm usually involves a set of parameters which togetger with the algorithm fully specify the jet definition. According to the remarks at the end of the previous section, jet algorithms should fulfill the following conditions

1. Infrared safety - the presence of additional soft particles should not affect the recombination of these particles into a jet.
2. Collinear safety - jet reconstruction should not depend on the fact, if the transverse momentum is carried by one particle, or if the particle is split into two collinear particles.

Two important steps must be defined in each jet algorithm

1. Clustering - description how the input objects are clustered into jets.
2. Recombination - determination of physical quantities of jets.

Additional steps may include the preclustering reducing the number of input objects for jet algorithm.

Two classes of jet algorithms are described here - cone algorithms and k_t algorithms. First of these algorithms is more illustrative, the second one is used in ATLAS. These algorithms use two different recombination schemes which description will follow. Detailed description as well as other jet algorithms can be found in [44, 45]. After the definition of jet algorithms a short description follows, how the objects (not necessary particles) with defined four-momenta are constructed from the signal observed on the ATLAS detector.

2.3.1 Cone algorithms

The first step of these algorithms is to order all input objects (reconstructed detector objects with four-momentum representation) in decreasing order of transverse momentum p_T. If the object with the highest p_T is above the seed threshold, all objects within a cone in rapidity y and azimuth ϕ with $\Delta R = \sqrt{\Delta y^2 + \Delta\phi^2} < R_{cone}$, where R_{cone} is the fixed cone radius, are recombined using Snowmass recombination scheme (see Section 2.3.3). A new cone is centered around a new direction and the objects in the new cone are recombined and again the direction is updated. This process continues until the direction of the cone does not change anymore after recombination, at which point the cone is considered stable and is called a proto-jet.

At this point, the next seed is taken from the input list and a new proto-jet is formed with the same iterative procedure. This continues until no more seeds are available.

The proto-jets found by this procedure can share some constituents. Constituents shared between two proto-jets are recombined into new proto-jet

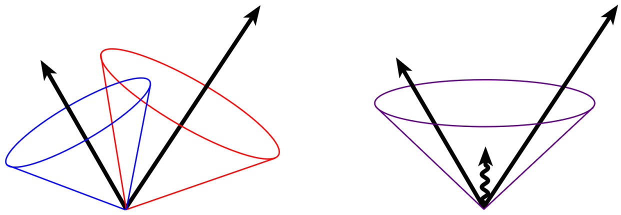

(a) Infrared unsafety

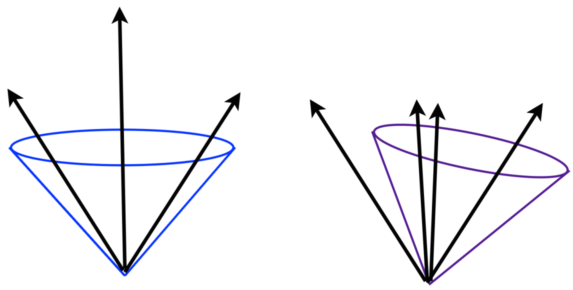

(b) Collinear unsafety

Figure 2.4: Illustration of (a) infrared unsafety and (b) collinear unsafety of fixed cone jet algorithm. Figures from [10].

and if the ratio $E_T^{shared}/\min(E_T^{neighbor}) > f$ is over the certain threshold for example $f = 0.5$ the neighboring proto-jets are recombined into one proto-jet (shared constituents are taken only once). If this condition is not satisfied, the shared constituents are assigned to the nearest proto-jet. When proto-jet does not share constituents it is recombined into the jet.

This algorithm is both not infrared safe (Figure 2.4a) and not collinear safe (Figure 2.4b). The infrared insensitivity can be improved by adding the midpoints between pairs of proto-jets fulfilling $R_{cone} < \Delta R < 2R_{cone}$ and repeating the iterative procedure with midpoints being new seeds. Since the collinear unsafety arises from the use of seed towers, Seedless cone algorithm was developed, which searches the entire detector to find all stable proto-jets.

Typical parameters used by fixed cone algorithm are a seed threshold of $p_T > 1\,\text{GeV}$, and a narrow ($R_{cone} = 0.4$) or a wide cone jet ($R_{cone} = 0.7$) option.

2.3.2 k_t algorithms

In this class of algorithms all pairs (i, j) of input objects are analyzed with respect to their relative transverse momentum squared, defined by

$$d_{ij} = \min\left(p_{T,i}^{2p}, p_{T,j}^{2p}\right)\frac{\Delta R_{ij}^2}{R^2} \tag{2.3}$$

and the squared p_T of object i relative to the beam axis

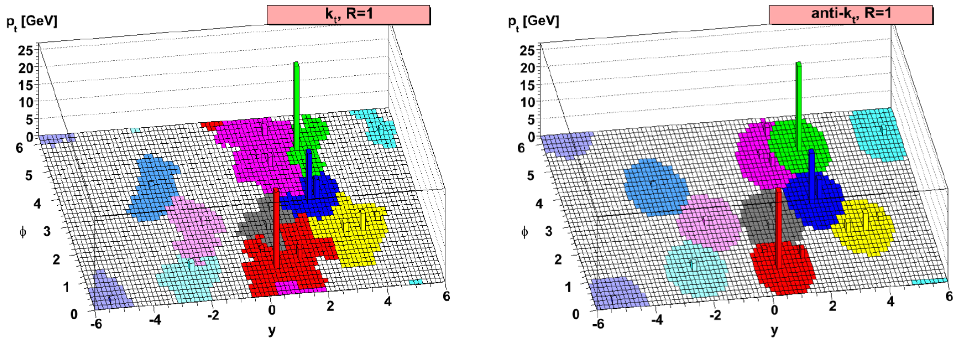

Figure 2.5: Illustration of k_t and anti-k_t jet algorithms with $R = 1$ for calorimeter signal towers in azimuth Φ and pseudorapidity y. Towers of the same color were recombined to one jet. Figure taken from [10].

$$d_i = p_{T,i}^{2p}. \tag{2.4}$$

Here $\Delta R_{ij}^2 = (y_i - y_j)^2 + (\phi_i - \phi_j)^2$ and $p_{T,i}$, y_i and ϕ_i are respectively the transverse momentum, rapidity and azimuth of particle i. In addition to the radius parameter R, parameter p was added to split k_t algorithms into three categories.

- $p = 1$ k_t algorithm,
- $p = 0$ Cambridge/Aachen algorithm,
- $p = -1$ anti-k_t jet-clustering algorithm.

These algorithms first find the minimum d_{min} of all d_{ij} and d_i. If d_{min} is in d_{ij}'s, the corresponding objects i and j are combined into a new object k using four-momentum recombination. Both objects i and j are removed from the list, and the new object k is added to it. If d_{min} is in d_i's, the object i is considered to be a jet by itself and is removed from the list.

This means that all original input objects end up to be either part of a jet or to be jets by themselves. Contrary to the cone algorithm described earlier, no objects are shared between jets and the procedure is both infrared and collinear safe.

ATLAS uses anti-k_t algorithm with $R = 0.4$ for narrow and $R = 0.6$ for wide jets. The differences between k_t-algorithms are detailed described in [46]. Recombination of calorimeter signal towers (see Section 2.3.4) in jets is for k_t and anti-k_t algorithms shown at Figure 2.5.

2.3.3 Recombination

Let J be the index set of the input objects with the defined four-momenta $(E^i, p_x^i, p_y^i, p_z^i)$, $i \in J$ which has to be recombined into the jet with new kinematic quantities E^J, $\mathbf{p}^J$, p_T^J, y^J, ... Possible recombination schemes are

- **Snowmass Scheme**
  Used by fixed cone algorithm when finding proto-jets.

$$E_T^J = \sum_{i \in J} E_T^i \quad , \quad \eta^J = \frac{1}{E_T^J} \sum_{i \in J} E_T^i \eta^i \quad , \quad \phi^J = \frac{1}{E_T^J} \sum_{i \in J} E_T^i \phi^i. \tag{2.5}$$

- **Four-Momentum Recombination (E-Scheme)**
  Used by k_t-algorithms and by fixed cone algorithm to final recombination of proto-jets into jets.

$$p^J = (E^J, \mathbf{p}^J) = \sum_{i \in J} (E^i, p_x^i, p_y^i, p_z^i), \tag{2.6}$$

$$p_T^J = \sqrt{(p_x^J)^2 + (p_y^J)^2} \quad , \quad y^J = \frac{1}{2} \ln \frac{E^J + p_z^J}{E^J - p_z^J} \quad , \quad \phi^J = \tan^{-1} \frac{p_y^J}{p_x^J}. \tag{2.7}$$

2.3.4 Calorimeter jets

The most important detectors for the jet reconstruction are the ATLAS calorimeters. The ATLAS calorimeter system has about 200,000 individual cells of various sizes and with different readout technologies and cell geometries. For jet finding it is necessary to first combine these cell signals into larger signal object with physically meaningful four-momenta. The two concepts available are the calorimeter signal towers and the topological cell clusters.

In the case of calorimeter signal towers, the cells are projected onto a fixed grid in pseudorapidity η and azimuth ϕ. The tower bin size is $\Delta\eta \times \Delta\phi = 0.1 \times 0.1$ in the whole acceptance region of the calorimeters, i.e. in $|\eta| < 5$ and $-\pi < \phi < \pi$ with approximately $100 \times 64 = 6,400$ towers in total.

The alternative representation of the calorimeter signals for jet reconstruction are topological cell clusters, which are basically an attempt to reconstruct three-dimensional "energy blobs" representing the showers developing for each particle entering the calorimeter. The clustering starts with seed cells with a signal-to-noise ratio, or signal significance $\Gamma = E_{cell}/\sigma_{noise,cell}$, above a certain threshold S, i.e. $|\Gamma| > S = 4$. All directly neighboring cells of these seed cells, in all three dimensions, are collected into the cluster. Neighbors of neighbors are considered for those added cells which have Γ above a certain secondary threshold N ($|\Gamma| > N = 2$). Finally, a ring of guard cells with signal significances above a basic threshold $|\Gamma| > P = 0$ is added to the cluster. After the initial clusters are formed, they are analyzed for local signal maxima by a splitting algorithm, and split between those maxima.

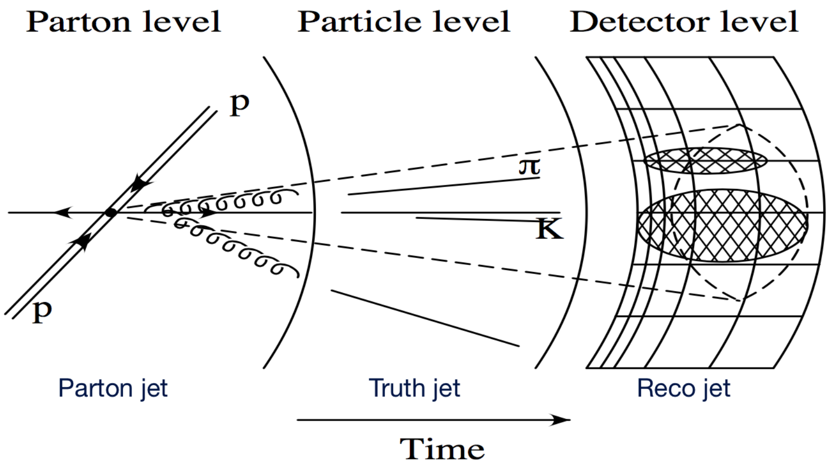

Figure 2.6: Three levels of jet reconstruction. Figure from [11]

2.4 Jet corrections

Before jets can proceed to the data analysis, corrections have to be applied to minimize detector effects including calorimeter non-compensation, noise, losses in dead material and cracks, longitudinal leakage and particle deflection in the magnetic field. Indispensable tool for jet corrections are Monte Carlo event generators - Pythia8 [47] generating high-energy-physics events and Geant4 [48] or AtlfastII [49] detector simulations for simulating the ALTAS detector response of Pythia8 generated events.

Using these tools it is possible to reconstruct jets from Monte Carlo events on three different stages of collision indicated in Figure 2.6. First there are parton jets which are reconstructed from the quarks, gluons and other elementary particles created just after the collision. Stable particles (with lifetime $c\tau \sim 10^{-15}\,\mathrm{m}$) created by hadronization are recombined into the truth jets. When collision reaches the detector, the detector simulation is used and the recorded signal is reconstructed into reco jets.

First, the reco jets are corrected to the truth jets leading to modification of kinematic properties of individual reco jet in the process called jet energy scale calibration.

2.4.1 Jet Energy Scale Calibration

Energy E_{reco} of the jet measured by the detector may differ from the energy E_{truth} of the corresponding particle jet. The goal of the jet energy scale calibration is to remove some detector effects and correct E_{reco} to E_{truth}. The detector effects can be summarized by the formula

$$E_{truth} = \frac{E_{reco} - O}{R \cdot S}, \tag{2.8}$$

where O is the offset representing subtraction of additional energy, which is represented by the detector noise and pile-up with contributions from other pp collisions occurring during beam crossing. Hadronic character of jets observed at LHC is the reason why the response R is the largest correction. Showering factor S describes the particle flow out/from jet recombination cells. More concise information about the parameters just introduced can be found in [11].

Because the calibration is persistently evolving, each jet analysis uses as the input the uncalibrated reco jets which are then easily calibrated using standard library ApplyJetCalibration [50].

However, there are some detector effects which can't be fixed by the calibration. These effects include the limited detector resolution (detector cells have finite dimensions) and the limited acceptance (not all events are recorded). The former leads to the smearing of jet kinematic properties wheres the later to decrease of observed cross section against the value theoretically predicted. Both of these effects are negatively affecting the observables and can be partially removed by the unfolding procedure, which unlike the jet calibration, is analysis dependent.

2.4.2 Unfolding

In this analysis, the distribution $f(p_T)$ of inclusive jet p_T is measured for $p_T \in \langle a, b \rangle$. Due to the detector imperfections, instead of physical variable p_T new variable x and its distribution $g(x)$ are measured. New distribution can be expressed as

$$g(x) = \int_a^b A(x, p_T) f(p_T) dp_T, \tag{2.9}$$

with the function $A(x, p_T)$ describing the detector response as can be seen when the detector is exposed to a particle beam with well known $p_T = p'_T$ meaning $f(p_T) = \delta(p_T - p'_T)$, leading to $g(x) = A(x, p'_T)$. The reconstruction of $f(p_T)$ from measured $g(x)$ is called unfolding.

For practical purposes the equation (2.9) should be discretized so instead of continuous distribution $g(x)$ the discretized values $g_i = \int_{N(i)} g(x)dx$ of discretized observable $f_i = \int_{N(i)} f(p_T)dp_T$ are measured, where the integration is done over measurable $N(i) \subset \langle a, b \rangle$. For simplicity assume $x \in \langle a, b \rangle$ is discretized in the same way as the physical p_T. Equation (2.9) then reads

$$g = Af, \tag{2.10}$$

with g and f being vectors of g_i's and f_i's respectively and A matrix derived from $A(x, p_T)$, later in Section 3.3 called the transfer matrix. If the limited acceptance would be the only detector problem, then A would be diagonal matrix with some elements < 1. When the limited resolution comes to play, the diagonal entries start to smear out of the diagonal and the matrix A starts to complicate.

The unfolding result which offers the solution of (2.10) by the inversion of matrix A is mostly disappointing as is illustrated e.g. in [51]. For result improvement, different unfolding methods were developed including Iterative Bayesian Unfolding [52], Singular Value Decomposition [53], or Iterative, Dynamically Stabilized (IDS) method [54], which is the method used in this thesis.

Chapter 3

Data Analysis

In physics, you don't have to go around making trouble for yourself - nature does it for you.

Frank Wilczek

QCD jets are the most common hard objects observed in the ultrarelativistic collisions at hadron colliders, with their cross section exceeding any other physics process by orders of magnitude. Measurement of inclusive jet cross section thus provides the test for both QCD predictions and the detector performance up to the momentum transfers not reachable by any other physics processes.

This chapter describes the details of the double differential inclusive jet cross section analysis.

3.1 Data Characteristics

Data used in this thesis are Monte Carlo generated events of pp collisions at the center-of-mass energy $\sqrt{s} = 13\,\mathrm{TeV}$ with PYTHIA8 [47] event generator using CT10 PDFs [55] and ATLAS underlying event tune AU2 [56]. QCD calculations are done only to the leading order in PYTHIA8. The response of the ATLAS detector on these events was calculated with GEANT4 [48] software toolkit.

Particles were recombined into jets using anti-k_t jet algorithm with parameter $R = 0.4$. There are particle jets reconstructed from the PYTHIA8 output, which further in this thesis are denoted truth jets, and next to them, there are the reco jets reconstructed from the output of GEANT4 detector simulation from the ATLAS detector topological cell clusters.

JZXW	p_T range (GeV)	Cross-section (fb)	Filter Efficiency	# envents
JZ0W	0 - 20	7.8420e+13	9.7193e-01	3498000
JZ1W	20 - 80	7.8420e+13	2.7903e-04	2998000
JZ2W	80 - 200	5.7312e+10	5.2261e-03	500000
JZ3W	200 - 500	1.4478e+09	1.8068e-03	499500
JZ4W	500 - 1000	2.3093e+07	1.3276e-03	477000
JZ5W	1000 - 1500	2.3793e+05	5.0449e-03	499000
JZ6W	1500 - 2000	5.4279e+03	1.3886e-02	493500
JZ7W	2000 +	9.4172e+02	6.7141e-02	497000

Table 3.1: The cross-sections (XS), filter efficiency (FE) and number of events for the JZXW samples which differ in the leading truth jet p_T range.

Reco jets were calibrated using ApplyJetCalibration [50] library version 3.28 with configuration parameters loaded from the `JES_Prerecommendation2015_Feb2015.` with calibration sequence `JetArea_Residual_EtaJES`. In next reco jets denotes the reco calibrated jets.

Events are generated in JZ slices according to the leading truth jet p_T. These samples differ in event weight which is for the whole event calculated as

$$\text{weight} = \frac{(\text{XS}) \cdot (\text{FE}) \cdot w_0}{(\#\ \text{events})}, \tag{3.1}$$

with XS beeing cross-section, FE filter efficiency and w_0 additional weight factor stored in `EventInfoAux` container. Concrete values for datasets used in this theses are given in Table 3.1.

Analysis uses jets with transverse momentum $p_T > 15\,\text{GeV}$ and rapidity $|y| < 4$ and is done in double binning in p_T and $|y|$ with the following edges which are the same as in the analysis from 2011/2012 [57].

$$\begin{aligned} p_T =& 15 - 20 - 25 - 35 - 45 - 55 - 70 - 85 - 100 - 116 - 134 - 152 - 172 - 194 - 216- \\ & 240 - 264 - 290 - 318 - 346 - 376 - 408 - 442 - 478 - 516 - 556 - 598 - 642- \\ & 688 - 736 - 786 - 838 - 894 - 952 - 1012 - 1076 - 1162 - 1310 - 1530- \\ & 1992 - 2300 - 2800 - 3400 - 4100 - 5000 - 6000 - 7200\,\text{GeV} \\ |y| =& 0.0 - 0.5 - 1.0 - 1.5 - 2.0 - 2.5 - 3.0 - 3.5 - 4.0 \end{aligned} \tag{3.2}$$

The edges in p_T are chosen to resolution in each bin was the same up to the systematic error.

3.2 Event Selection

In this section the jet selection criteria and matching of truth with reco jets are described. The former is needed to cut those jets (or those events) off, which were misinterpreted by the detector, by the later the inputs for the unfolding procedure are obtained. Description of the unfolding procedure will follow in the next section. More details including graphical display and numerical results for procedures described in this section are given in Appendix A.

3.2.1 Jet Cuts

- **$\mathbf{p_T}$ Cut**

  Reco and truth jets with $p_T > 15\,\text{GeV}$ were kept.

- **y Cut**

  Reco and truth jets with $|y| < 4$ were kept.

- **Zero jet (0-jet) Cut**

  Only those events which has at leas one reco or one truth jet left proceeded further in the analysis.

- **Leading Ration (LR) Cut**

  In this cut the reco and truth jets with the highest p_T were used. If there was only one reco jet left, the ratio $LR = p_T^{reco,leading}/p_T^{truth,leading}$ was calculated. If there were two reco jets, instead of $p_T^{reco,leading}$ the average p_T of two leading reco jets was calculated. If $0.6 < LR < 1.4$ the event was assumbed by the analysis.

Numbers of reco and truth jets removed in each step are shown in Table A.1, where also the cut efficiencies for individual JZXW samples are shown. The impact of each cut on jet p_T spectrum of reco and truth jets is displayed in Figure A.1.

It can be seen that the most important cut is the 0-jet cut which removes approximately 80 % of reco jets in JZ0W sample whereas the truth jets remain intact. According to Table 3.1 for event from the JZ0W sample the leading truth jet $p_T < 20\,\text{GeV}$ which has no longer to hold for reco jets which were in some cases reconstructed with $p_T \sim 100\,\text{GeV}$. Because of Monte Carlo event weight of events from JZ0W sample is dominant over event weights of other JZXW samples by several orders, the misreconstructed reco jets from JZ0W sample were parasitizing on the observed p_T spectrum of reco jets as can be seen from top of the Figure A.1.

3.2.2 Jet Matching

To find, how the truth jets are reconstructed by the detector, the jet matching has to be done, i.e. for each truth jet it is needed to find corresponding reco jet which should correspond to the original truth jet reconstructed by the detector. Jet matching used in this thesis is based on minimal angular distance between matched and its description follows in this section.

For each pair (i, j) of reco and truth jet, the quantity $dR_{ij} = \sqrt{d\phi_{ij}^2 + dy_{ij}^2}$ was calculated with $d\phi_{ij}$ being angle between ϕ_i^{reco} and ϕ_j^{truth} and $dy_{ij} = y_i^{reco} - y_j^{truth}$. The minimum was found between all of dR_{ij}'s. If this was smaller than the defined cutoff $\min(dR_{ij}) = dR_{pq} < dR^{cutoff} = 0.2$, the jets (p, q) were matched and further not assumed in matching procedure. This continued until condition $\min(dR_{ij}) < dR^{cutoff}$ was not satisfied or all of the reco or truth jets were matched.

Numbers of reco and truth jets, both matched and unmatched are shown in Table A.1 where also the matching efficiencies for individual JZXW samples are shown. In Figure A.2 p_T spectra of matched and unmatched reco and truth jets are compared with p_T spectra of all reco and truth jets respectively. Figure A.3 shows the p_T spectra of reco and truth jets after event selection for all rapidity bins assumed in this analysis.

It can be seen that for JZ(1-7)W samples, there is much more unmatched reco jets, than is the unmatched truth jets. Looking back at the statistics of the p_T cut, the reason is, that more than a half of truth jets has $p_T < 15\,\text{GeV}$ in every JZXW sample, which does not hold for the reco jets. There is much more reco jets in statistics than is the truth jets.

From the top of the Figure **??** showing the contribution of matched jets to p_T spectra, it can be seen, that starting with $p_T > 25\,\text{GeV}$, p_T spectra of reco jets overwhelms those of truth jets. Taking into account the fact, that p_T spectra of matched reco and matched truth jets are obtained from the same number of jets, this can seem to be a little bit confusing. The reason is, that some reco jets overflow the p_T range defined by the JZXW sample and that each event is filled with weight defined by the JZXW sample, which with increasing p_T falls down.

3.3 Unfolding

Summarizing the results of the previous section, firstly the series of four cutoffs was done on all events saved in Monte Carlo simulated data and the sets of jets denoted reco and truth jets were obtained. Both reco and truth jets were split into two categories depending on successful matching - there is correspondence $1:1$ between matched reco and matched truth jets. Reco jets, which were not matched, formed the unmatched reco jets, and similarly a set of unmatched truth jets was created. All these 6 sets of jets are needed

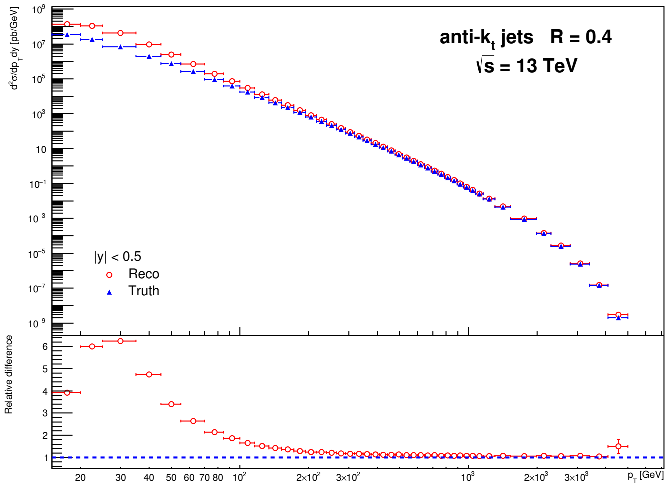

Figure 3.1: Comparison of p_T spectra of reco and truth jets after event selection. Each bin was divided by its width and all corresponding rapidity bins were merged to this histogram so y-axis has physical meaning of differential cross section in p_T. Bottom graph contains the relative difference between reco and truth differential cross section in p_T.

by the unfolding procedure which description follows in this section.

Figure 3.1 shows the p_T spectra of reco and truth jets. It can be seen, that observed p_T spectrum, represented by the reco jets, differs from the p_T spectrum theoretically expected which is represented by the p_T spectrum of truth jets. Unfolding should transform the observed p_T spectrum to the spectrum theoretically expected. If this transformation would be done on real data, it should ideally preserve additional structures, which are presented in data, but not included by the theory.

The main ingredient for the unfolding procedure is the transfer matrix A_{ij} which contains the number of reco jets in bin i with a matched truth jet that was generated in bin j and describes thus the smearing effects of the detector. In this thesis the double binning 3.2 is used which complicates the situation because the matched reco jet can simply migrate of the transfer matrix from Figure 3.2, when its rapidity $|y| > 0.5$ and when it was matched with truth jet with $|y| < 0.5$ or vice versa. Two ways of dealing with double binning are assumed in this thesis.

1. **Simple unfolding**

   In this case, only those reco and truth jets was used in the transfer matrix, which were matched within the same rapidity bin. Remaining matched jets were added to the unmatched statistic. 8 transfer matrices 46×46 is filled (one for each rapidity bin, 46 = number of p_T bins) and unfolding is done for each of these matrices separately. One of these matrices for $|y| < 0.5$ rapidity bin is shown at Figure 3.2.

2. **2D unfolding**

   In this case, the unfolding matrix was redefined to encapsulate the matching of jets between two different rapidity bins. In this case only one transfer matrix 368×368 is created ($368 = 46 \cdot 8$) with unfolding being done only for this matrix shown at Figure 3.3, from which the way how the transfer matrix was redefined from the simple unfolding should follow.

Transfer matrix from Figure 3.3 used by the 2D unfolding contains at the diagonal 8 submatrices which are the unfolding matrices used by the simple unfolding. Next to these diagonal submatrices transfer matrix of 2D unfolding contains 14 additional submatrices beside diagonal. These corresponds to the matched jets with migration in rapidity bins and in case of simple unfolding, these jets are assumed to be unmatched.

Dominant elements of each of the submatrices are on the main diagonal, which corresponds to the fact, there is no significant bias in p_T reconstruction. The finite p_T resolution causes the smearing of the diagonal and finite rapidity resolution is the cause of the 14 minor submatrices.

Next to the transfer matrix, numbers of matched and unmatched reco and truth jets are needed for each (y, p_T) bin by unfolding procedure. These serve for calculation of matching efficiency which is the key ingredient in the first and the last step of unfolding procedure. Matching efficiencies for $|y| < 0.5$ rapidity bin are for both simple and 2D unfolding shown at Figure 3.4 and for other rapidity bins, the results are shown in Appendix B.1

Unfolding procedure can be divided into three main steps

1. Input data are multiplied by the matching efficiency of signal jets.

2. Transfer matrix is used to correct data spectrum for detector effects. For this purpose, the Iterative Dynamical Stabilized (IDS) [54] unfolding method was used which uses the series of iterations to improve unfolding results. In this thesis the iteration was done once.

3. Spectrum obtained by the step 2 is divided by the matching efficiency of truth jets in order to correct resulting spectrum for the unmatched truth jets.

Figure 3.5 shows the comparison of p_T spectra of signal jets and unfolded spectrum (by 2D unfolding method) with the p_T spectrum of truth jets (left) and the comparison of simple and 2D unfolded spectra with the spectrum of truth jets (right) for $|y| < 0.5$ rapidity bin. Results for all rapidity bins are shown in Appendix B.2.

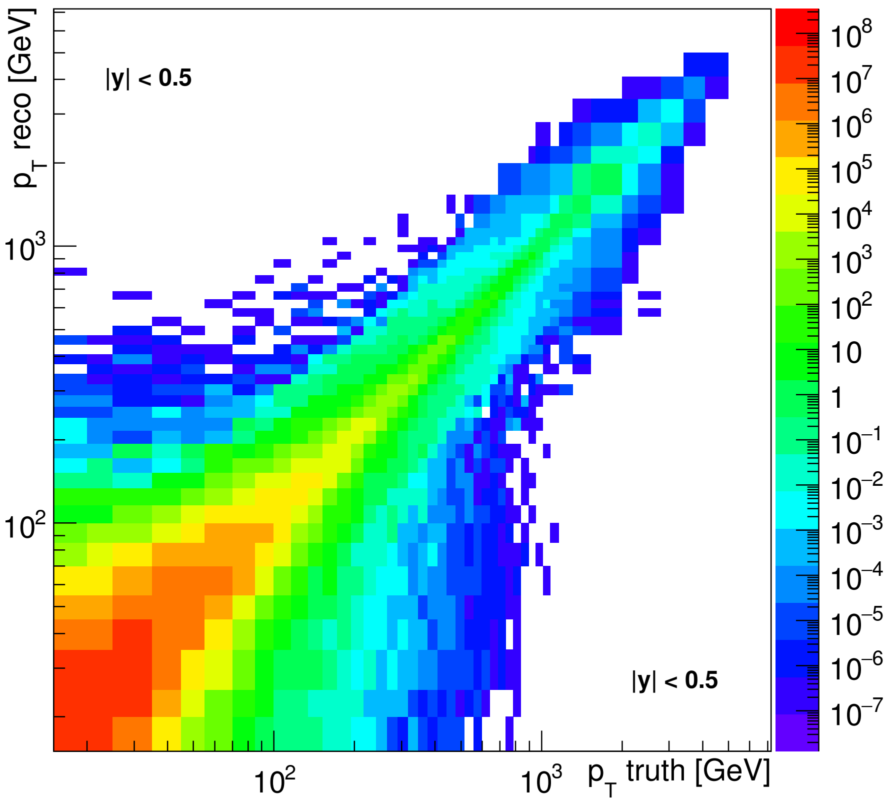

Figure 3.2: Unfolding matrix for matched reco and truth jets with rapidity $|y| < 0.5$ corresponding to one of eight matrices used in the simple unfolding. Each cell is proportional to the number of jets with truth p_T in range determined by the x-axis which were reconstructed to the reco jets with p_T determined by the y-axis. White space signalize no input.

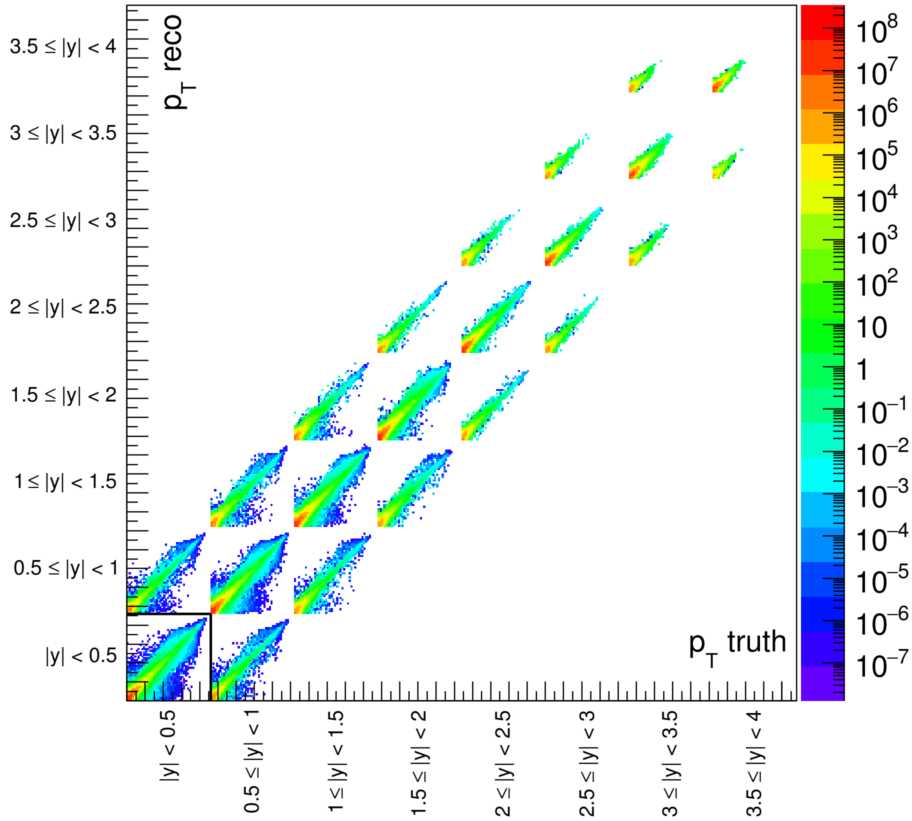

Figure 3.3: Unfolding matrix used in the 2D unfolding. Each cell is proportional to the number of jets with truth p_T and rapidity y determined by the x-axis, which were reconstructed to the reco jets with p_T and y determined by the y-axis. Marked square in $|y| < 0.5$ region is the matrix shown in Figure 3.2. Projection of this matrix on the x and y-axis corresponds to the p_T spectrum of matched truth and reco jets for corresponding rapidity bin respectively.

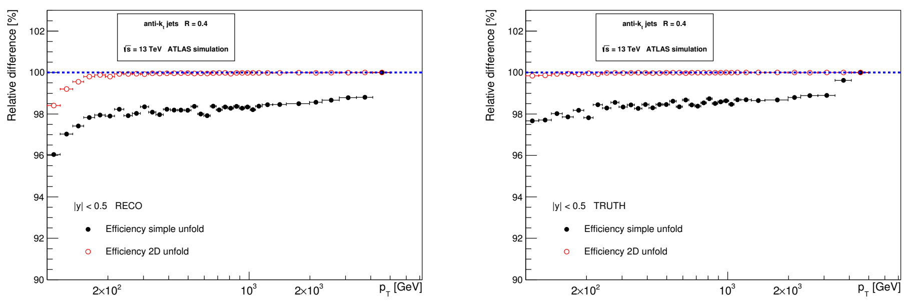

Figure 3.4: Comparison of matching efficiency of simple and 2D unfolding for $|y| < 0.5$ rapidity bin. Matching efficiency is compared for both reco jets (left) and truth jets (right). Matching efficiency for all rapidity bins is shown in Appendix B.1.

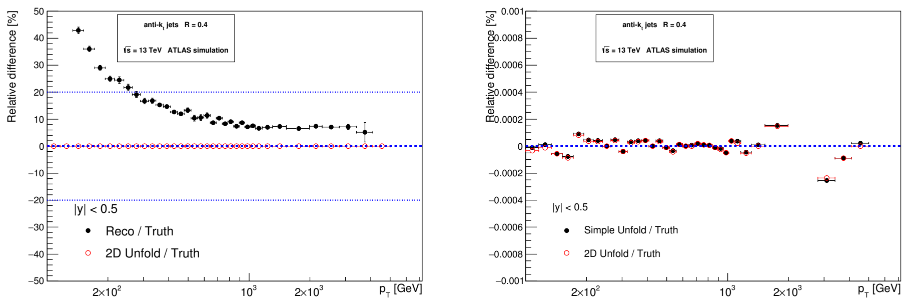

Figure 3.5: Comparison of p_T spectra of signal jets and the unfolded p_T spectra (2D unfolding) with the p_T spectra of the truth jets (left). Comparison of unfolded spectra obtained by the 2D and simple unfolding with the p_T spectra of the truth jets (right). Both graphs are for $|y| < 0.5$ rapidity regions. Results for all rapidity bins are shown in Appendices B.2, B.3.

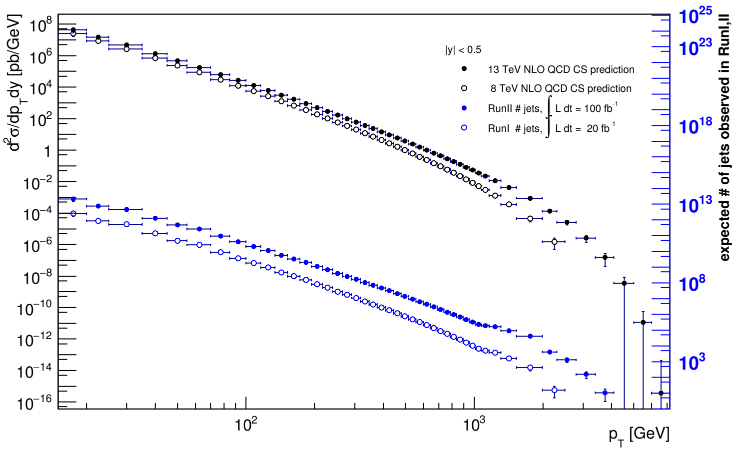

Figure 3.6: Comparison of NLO QCD prediction of double differential inclusive jet cross section (black) for pp collisions at $\sqrt{s} = 13\,\text{TeV}$ (filled circles) corresponding to the LHC Run II and $\sqrt{s} = 8\,\text{TeV}$ (empty circles) corresponding to the LHC Run I. The cross section is multiplied by integrated luminosities and p_T bin width to obtain the expected number of jets observed in each p_T bin (blue). Figure shows only $|y| < 0.5$ rapidity bin, remaining rapidity bins are shown in Appendix C.1.

From figures it follows, the unfolding procedure corrects the p_T spectrum of reco jets to p_T spectrum of truth jets up to the systematic error $< 10^{-3}\,\%$ and that the differences between results of simple and 2D unfolding are even smaller.

3.4 Comparison with NLO Prediction

The unfolded p_T spectrum obtained in the previous section, was compared with the p_T spectrum obtained by the NLO QCD calculations. These calculations was done with NLOJET++ program v4.1.2 [58] using CT10 NLO PDF set [55].

NLO predictions were compared for two different center-of-mass energies of pp collisions - first corresponding to the LHC Run I ($\sqrt{s} = 8\,\text{TeV}$) and second to Run II ($\sqrt{s} = 13\,\text{TeV}$). This comparison is shown for $|y| < 0.5$ rapidity bin in Figure 3.6, where also the differential cross section is multiplied by the p_T bin width and by the integrated luminosity of Run I ($20\,\text{fb}^{-1}$) and expected integrated luminosity of Run II ($100\,\text{fb}^{-1}$) to obtain expected number of jets observed in each p_T bin. Comparisons for other rapidity bins are shown in Appendix C.1.

It can be seen, that the increase in the center-of-mass energy is the most significant for jets with high p_T. By the NLO QCD theoretical computations, several uncertainties are taken into account. These include [57]

- **Scale uncertainty**

  Coming from the choice of renormalization and factorization scales, including neglecting the higher order terms beyond NLO and making choice in scale, where the hard processes are replaced by hadronisation.

- α_S **uncertainty**

  Because α_S is experimentally determined with error as is shown in Figure with running coupling constant 1.8.

- **PDF uncertainty**

  Prediction depends on the concrete choice of PDF.

- **Nonperturbative corrections uncertainty**

  ???

- **Electroweak corrections uncertainty**

  Next to the QCD processes, the electroweak processes has to be assumed. These processes becomes more important, as the momentum transfer increases.

In this analysis, only first three of these corrections are assumed. The corrections were extracted from the files with NLO QCD predictions, where each correction is represented by the set of equally likely histograms differing from the default prediction. Correction was determined as the square sum of all the corrections up and down separately and for $|y| < 0.5$ rapidity bin are shown at Figure 3.7, other rapidity bins are shown in Appendix C.2.

Comparison of p_T spectra of truth jets with NLO QCD prediction is for $|y| < 0.5$ rapidity bin shown at Figure 3.8 for other rapidity bins see Appendix C.3.

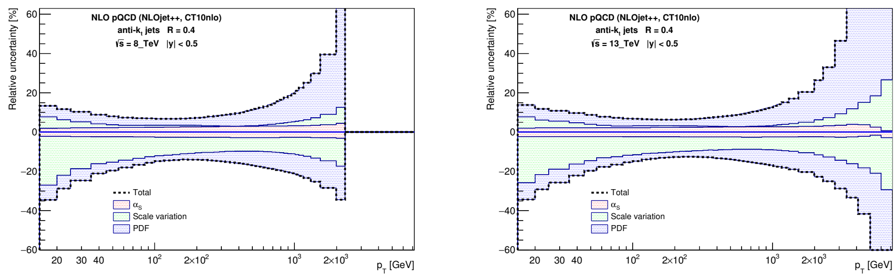

Figure 3.7: NLO uncertainties for NLO QCD predictions of inclusive jet differential cross section for pp collisions at $\sqrt{s} = 8\,\text{TeV}$ (left) and $\sqrt{s} = 13\,\text{TeV}$ (right) for $|y| < 0.5$ rapidity bin. Uncertainties for other rapidity bins are shown in Appendix C.2.

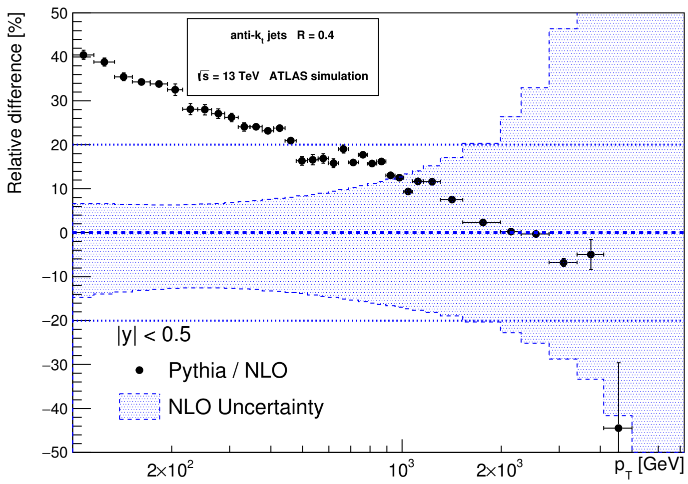

Figure 3.8: Comparison of Pythia8 prediction with NLO QCD prediction of inclusive jet double differential cross section for $|y| < 0.5$ rapidity bin with uncertaintis of NLO QCD predictions symbolized by the blue area. Comparisons for other rapidity bins are shown in Appendix C.3.

Conclusion

This thesis deals with the measurement of the inclusive jet double differential cross section in p_T and rapidity. Inclusive jets are dominant objects created by the ultrarelativistic collisions at Large Hadron Collider (LHC) with p_T covering range from a few GeV to a few TeV. Nowhere is the increase in the center-of-mass energy appreciated as is in the case of inclusive jets as it can be seen from Figure 3.6 According to the preliminary analysis, the pp collision in LHC Run II with the center-of-mass energy $\sqrt{s} = 13\,\mathrm{TeV}$ could create a thousands of jets with $1\,\mathrm{TeV} < p_T < 4\,\mathrm{TeV}$.

Inclusive jets are theoretically straightforward and hence powerful test of perturbative Quantum chromodynamics (pQCD) and with wide range of momentum transfers, the inclusive jet cross section is sensitive to the properties of the running coupling constant α_S. Momentum transfers in orders of $\sim 1\,\mathrm{TeV}$ will probe the structure of proton at small distance scales $\lambda \sim 1/p_T \sim \mathrm{TeV}^{-1} \sim 10^{-19}\,\mathrm{m}$ and will contribute to our understanding of the proton structure (parton distribution functions (PDF)). If there is new physics at these scales (such as the structure of quark), the inclusive jets may reveal it.

After an introduction, thesis begins with a brief description of the Quantum Chromodynamics (QCD) as one of the parts of the Standard Model (SM) following its historical development during which description the key concepts of QCD are introduced. These include the PDFs, running coupling constant α_S and asymptotic freedom phenomenons, leading to splitting QCD into perturbative and non-perturbative regions.

LHC with the ATLAS detector are described in the second chapter in which the key concept of this thesis - the jet - is defined. This include the description of jet algorithms with emphasize on anti-k_t jet algorithm relevant for this thesis and the procedure which must be done to detector recorded signal could be compared with the theoretical predictions of QCD leading to inevitable definitions of jet calibration and unfolding procedures.

The last chapter describes the analysis of double differential inclusive jet cross section in p_T and rapidity. As the input data, the PYTHIA8 generated events of pp collisions with center-of-mass energy $\sqrt{s} = 13\,\mathrm{TeV}$ using CT10 PDFs and ATLAS underlying event tune AU2. These data provided the detector and particle level jets, which were reconstructed using anti-k_t jet algorithm with $R = 0.4$. Jet energy scale calibration is done on detector level jets and p_T spectrum obtained after event selection is unfolded on particle level.

Two different approaches to unfolding were used - simple unfolding which matches jets only within the same rapidity bin and 2D unfolding which allows the migration of matched jets between different rapidity bins. These approaches differ in definitions of transfer matrices and in matching efficiencies which are shown in Appendix B.1. It can be seen the matching efficiency in case of simple unfolding is $\sim 2-5\,\%$ worse than the matching efficiency in 2D unfolding. This should cause the unfolded spectrum from simple unfolding will be more precise than that of 2D unfolding.

The results from both of the unfolding approaches are compared with the p_T spectrum of particle level jets in Appendix B.3. It can be seen, that in both cases, the unfolded p_T spectrum is in agreement with the p_T spectrum of particle level jets up to systematic error $< 10^{-3}\,\%$ and that the relative difference between two unfolding approaches is even smaller.

The second input for this analysis are the next-to-leading (NLO) order perturbative QCD predictions of double differential inclusive jet cross section in p_T and rapidity for center-of-mass energies $\sqrt{s} = 8\,\mathrm{TeV}$ (corresponding to LHC Run I) and $\sqrt{s} = 13\,\mathrm{TeV}$ (Run II) calculated using NLOJET++ program using the same parton distribution functions as PYTHIA8. In predictions the uncertainties in coupling constant α_S, PDFs and factorization and normalization scales are included. These uncertainties are shown in Appendix C.2.

Cross section predictions for $\sqrt{s} = 8\,\mathrm{TeV}$ and $\sqrt{s} = 13\,\mathrm{TeV}$ are compared in Appendix C.1 where with the usage of integrated luminosities $L = 20\,\mathrm{fb}^{-1}$ (Run I) and $L = 100\,\mathrm{fb}^{-1}$ (Run II expected) the numbers of jets expected to be observed in each p_T bin were calculated. It can be seen, that according to this prediction, in Run II ~ 1000 times more jets with $p_T > 1\,\mathrm{TeV}$ will be observed than it was in Run I. In addition LHC run II could create a few jets with $p_T \sim 4\,\mathrm{TeV}$.

p_T spectrum of particle jets obtained from PYTHIA8 is compared with p_T spectrum of parton jets from NLO prediction in Appendix C.3. Only for few highest p_T bins the cross section predicted by the NLO is bigger than that of PYTHIA8 whereas for low p_T the situation is opposite. The explanation for this behavior lies in hadronization, by which the original parton jet with high p_T can split into two or more jets with smaller p_T's.

There are several ways to extend this analysis. Although this analysis is only preparation for the analysis of real data which will be collected in LHC Run II, the implementations of the IDS unfolding method developed could serve for unfolding of the real p_T spectra measured by the ATLAS detector in Run II. The unfolding results could be further improved by the running on new datasets generated by the PYTHIA8 with the usage of newer parton density functions. The NLO prediction should be improved by the assuming the electroweak and non-perturbative corrections.

Appendices

Appendix A

Cut and Match Results

A.1 Cut Results

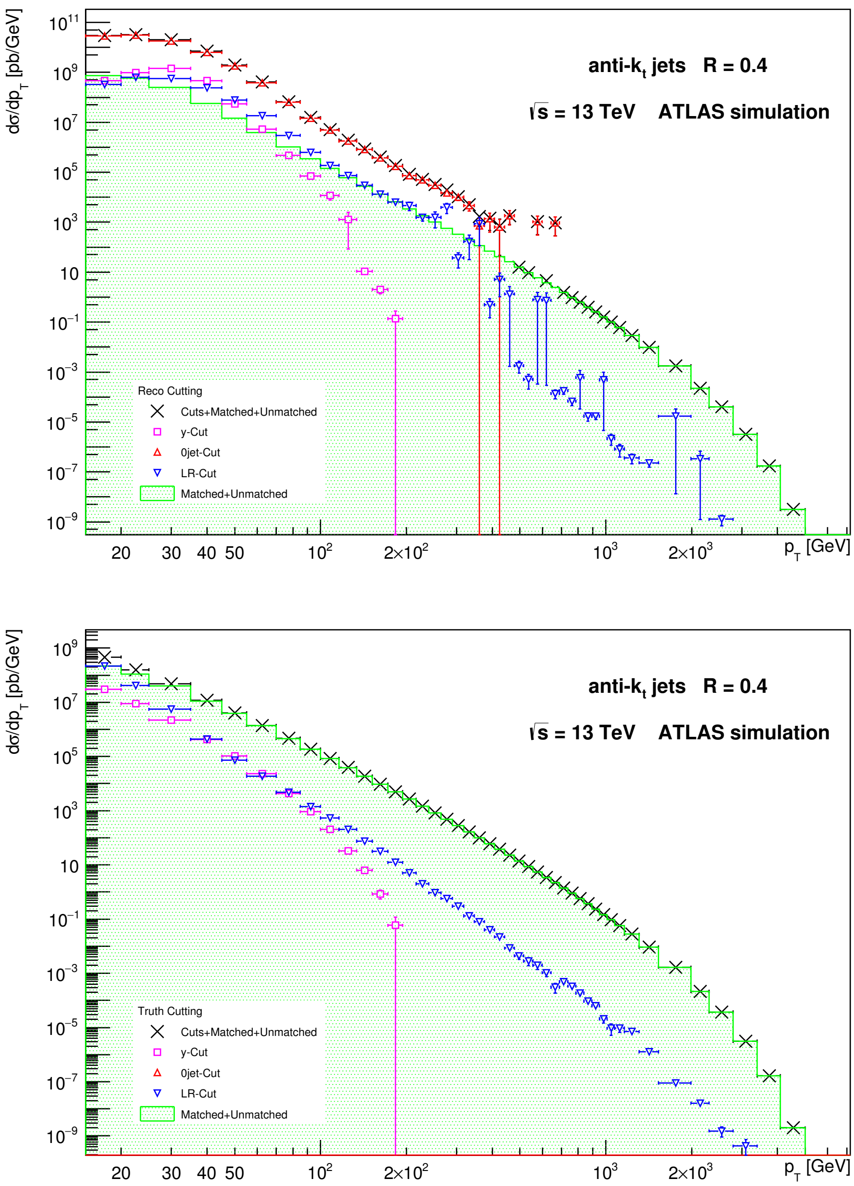

Figure A.1: Impact of 4 cuts defined in Section 3.2.1 on differential cross section in p_T of signal jets (top) and truth jets (bottom). Black dots represent the original uncutted spectrum, green area then these jets, which survived all four cutoffs.

A.2 Match Results

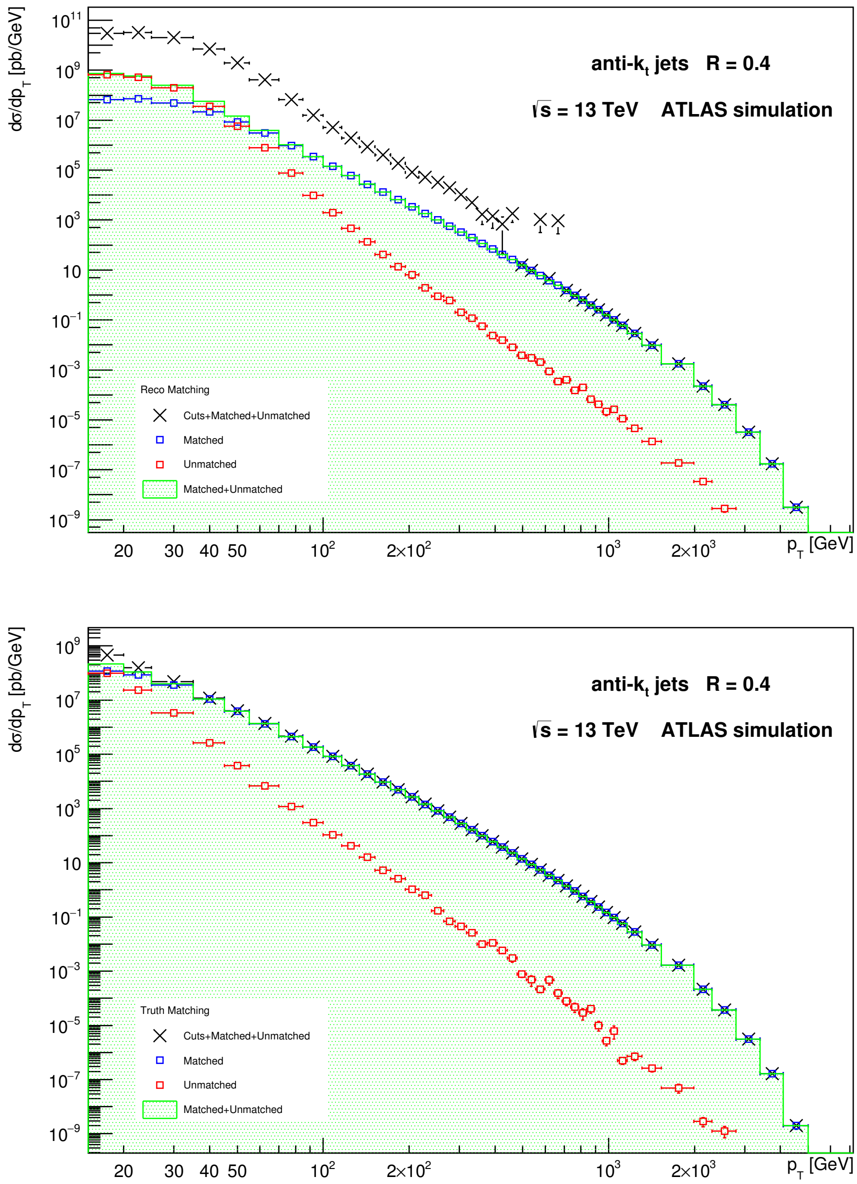

Figure A.2: Results of matching procedure described in Section 3.2.2 demonstrated on differential cross section in p_T of signal (top) and truth (bottom) jets. Black dots represent the original uncutted spectrum. The contribution of matched and unmatched jets to green area representing all jets which survived cutoffs is shown.

A.3 Truth and Reco p_T Spectra

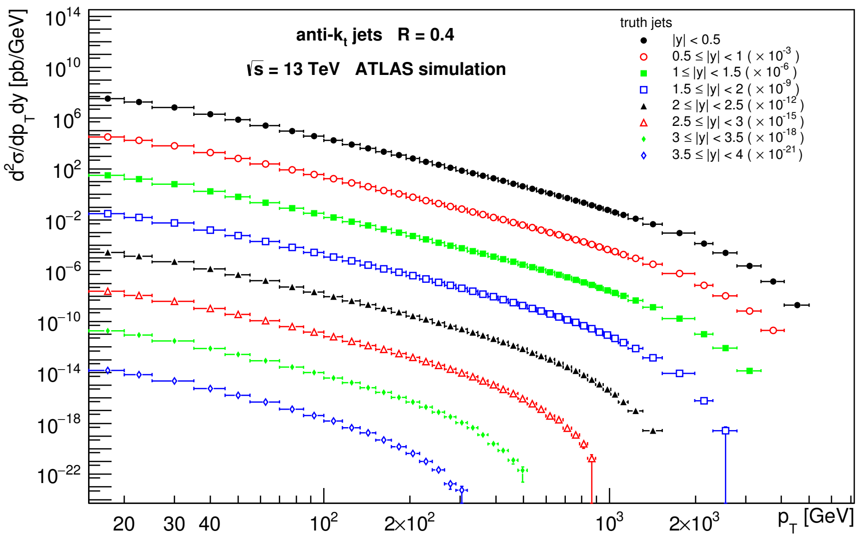

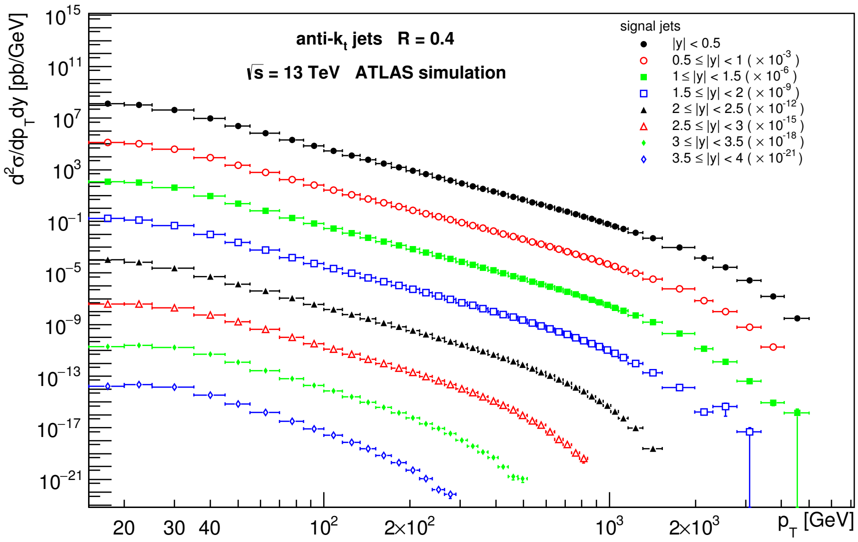

Figure A.3: Inclusive jet cross section of truth (top) and reco (bottom) jets as the function of jet p_T and rapidity. For the convenience the cross sections for different rapidity bins are multiplied by the factor indicated in the legend. Jets were identified with anti-k_t jet algorithm with $R = 0.4$.

# jets		**ALL**	JZ0W	JZ1W	JZ2W	JZ3W	JZ4W	JZ5W	JZ6W	JZ7W
Signal		**1.09e+08**	3.11e+07	3.59e+07	6.67e+06	7.07e+06	6.28e+06	7.29e+06	7.13e+06	7.11e+06
Truth		**7.28e+07**	3.04e+06	3.00e+07	6.17e+06	6.91e+06	6.20e+06	6.98e+06	6.53e+06	6.25e+06
CutPt	Signal	**9.36e+06** **8.6 %**	3.74e+06 12.0 %	3.13e+06 8.7 %	6.50e+05 9.7 %	5.87e+05 8.3 %	4.76e+05 7.6 %	5.48e+05 7.5 %	5.52e+05 7.7 %	5.63e+05 7.9 %
	Truth	**4.70e+07** **64.6 %**	3.00e+06 98.7 %	2.20e+07 73.1 %	3.86e+06 62.6 %	4.00e+06 57.8 %	3.42e+06 55.1 %	3.74e+06 53.6 %	3.43e+06 52.5 %	3.23e+06 51.6 %
Cuty	Signal	**3.43e+06** **3.1 %**	1.19e+06 3.8 %	1.29e+06 3.6 %	1.42e+05 2.1 %	1.28e+05 1.8 %	1.03e+05 1.6 %	1.16e+05 1.6 %	1.10e+05 1.5 %	1.08e+05 1.5 %
	Truth	**5.06e+05** **0.7 %**	3.04e+03 0.1 %	3.19e+05 1.1 %	4.54e+04 0.7 %	3.79e+04 0.5 %	2.88e+04 0.5 %	2.78e+04 0.4 %	2.22e+04 0.3 %	1.83e+04 0.3 %
Cut0jet	Signal	**2.64e+07** **24.2 %**	2.59e+07 83.2 %	5.70e+05 1.6 %	0.00e+00 0.0 %	0.00e+00 0.0 %	0.00e+00 0.0 %	0.00e+00 0.0 %	0.00e+00 0.0 %	0.00e+00 0.0 %
	Truth	**0.00e+00** **0.0 %**	0.00e+00 0.0 %	0.00e+00 0.0 %	0.00e+00 0.0 %	0.00e+00 0.0 %	0.00e+00 0.0 %	0.00e+00 0.0 %	0.00e+00 0.0 %	0.00e+00 0.0 %
CutLR	Signal	**4.09e+06** **3.7 %**	2.38e+05 0.8 %	3.82e+06 10.6 %	2.99e+04 0.4 %	7.07e+03 0.1 %	2.33e+03 0.0 %	1.63e+03 0.0 %	7.14e+02 0.0 %	6.31e+02 0.0 %
	Truth	**5.40e+05** **0.7 %**	2.19e+04 0.7 %	4.96e+05 1.7 %	1.82e+04 0.3 %	4.45e+03 0.1 %	1.33e+03 0.0 %	9.03e+02 0.0 %	4.37e+02 0.0 %	2.78e+02 0.0 %
Matched	Signal	**2.17e+07** **19.8 %**	7.62e+03 0.0 %	6.03e+06 16.8 %	1.95e+06 29.3 %	2.54e+06 36.0 %	2.46e+06 39.1 %	2.88e+06 39.5 %	2.78e+06 38.9 %	2.72e+06 38.2 %
	Truth	**2.17e+07** **29.8 %**	7.62e+03 0.3 %	6.03e+06 20.1 %	1.95e+06 31.7 %	2.54e+06 36.8 %	2.46e+06 39.6 %	2.88e+06 41.3 %	2.78e+06 42.5 %	2.72e+06 43.5 %
Unmatched	Signal	**4.42e+07** **40.5 %**	5.36e+04 0.2 %	2.10e+07 58.6 %	3.89e+06 58.4 %	3.81e+06 53.8 %	3.24e+06 51.6 %	3.75e+06 51.4 %	3.69e+06 51.8 %	3.72e+06 52.3 %
	Truth	**3.07e+06** **4.2 %**	6.18e+03 0.2 %	1.25e+06 4.2 %	2.89e+05 4.7 %	3.29e+05 4.8 %	2.95e+05 4.8 %	3.29e+05 4.7 %	3.03e+05 4.6 %	2.88e+05 4.6 %

Table A.1: Statistics for matching and cutting procedures described in Sections 3.2.1 and 3.2.2 displayed for all jets and for individual JZXW samples defined in Table 3.1. At the top, there is number of initial signal and truth jets respectively. For each cut, there is shown the number of jets, which were killed by it, and their relative number according to the original number of signal or truth jets respectively. Last two lines show the statistics of matching procedure including number of jets which were (un)matched.

Appendix B

Unfolding

B.1 Matching Efficiency

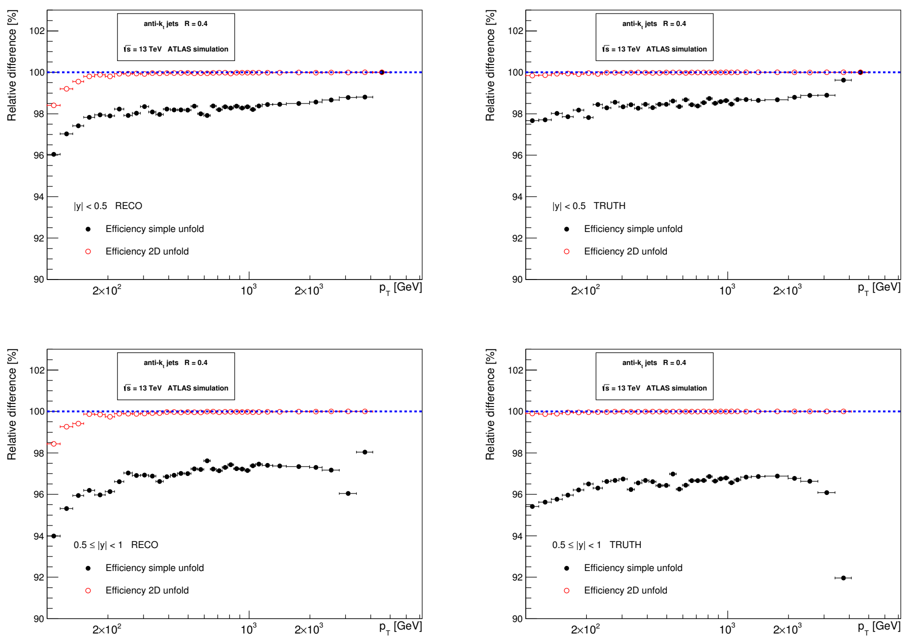

Figure B.1: Comparison of matching efficiencies of simple and 2D unfolding for $|y| < 0.5$ (top) and $0.5 \leq |y| < 1$ (bottom) rapidity bins. Matching efficiencies are shown for both reco jets (left) and truth jets (right).

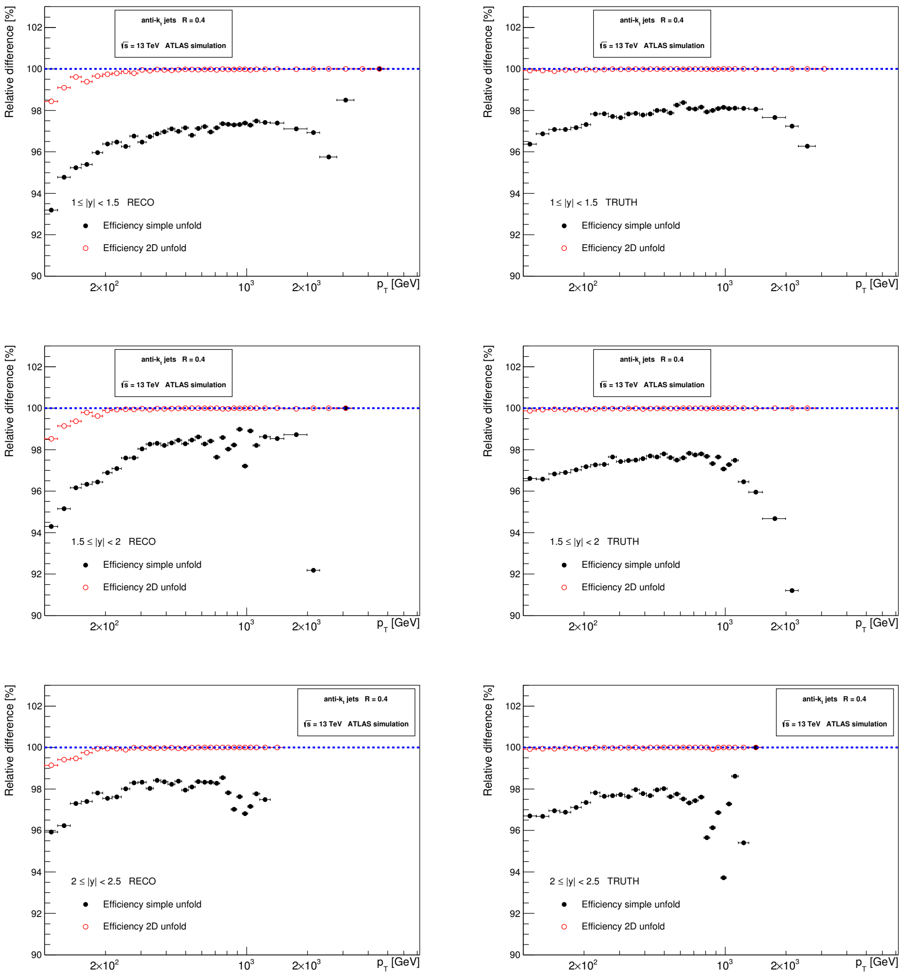

Figure B.2: Comparison of matching efficiencies of simple and 2D unfolding for $1 \leq |y| < 1.5$ (top), $1.5 \leq |y| < 2$ and $2 \leq |y| < 2.5$ (bottom) rapidity bins. Matching efficiencies are shown for both reco jets (left) and truth jets (right).

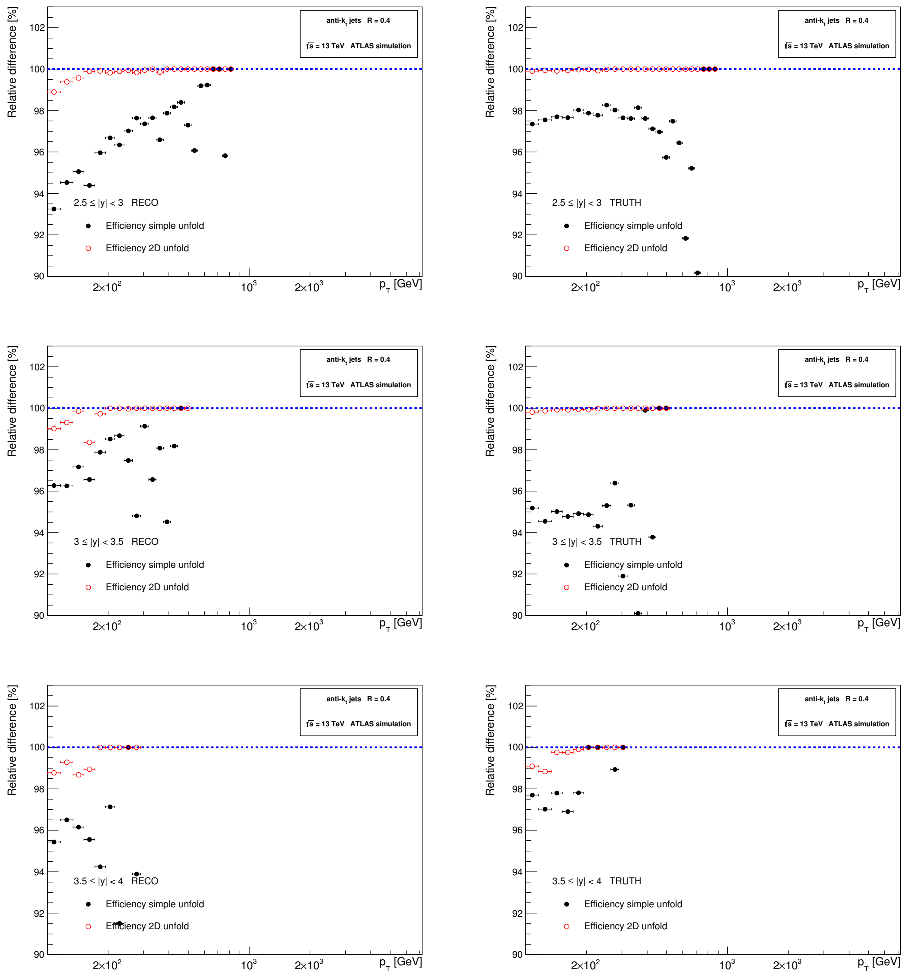

Figure B.3: Comparison of matching efficiencies of simple and 2D unfolding for $2.5 \leq |y| < 3$ (top), $3 \leq |y| < 3.5$ and $3.5 \leq |y| < 4$ (bottom) rapidity bins. Matching efficiencies are shown for both reco jets (left) and truth jets (right).

B.2 Unfolding Results

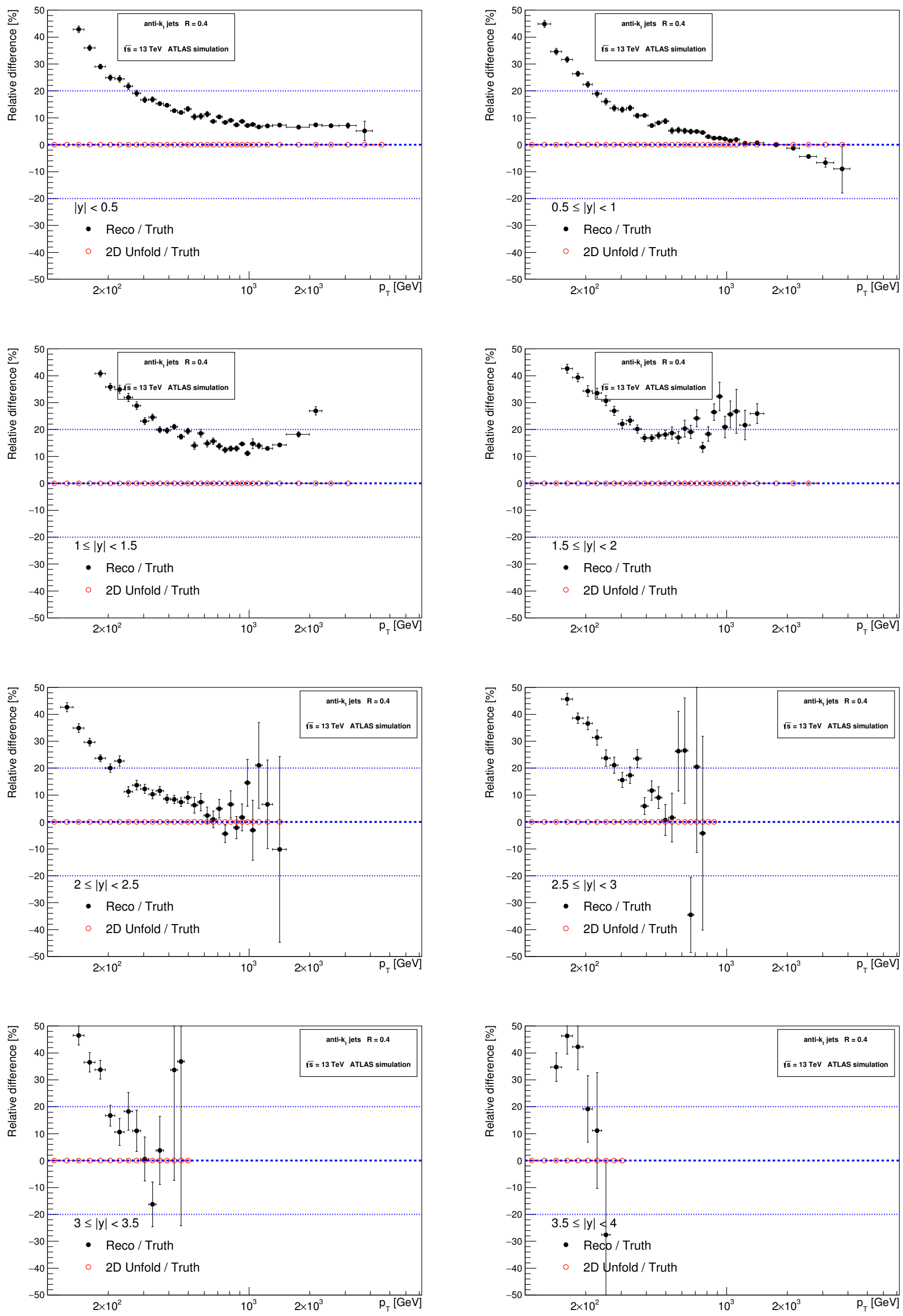

Figure B.4: Comparison of p_T spectra of reco jets and the unfolded p_T spectra (2D unfolding) with the p_T spectra of the truth jets for 8 different rapidity bins.

B.3 Simple and 2D Unfolding

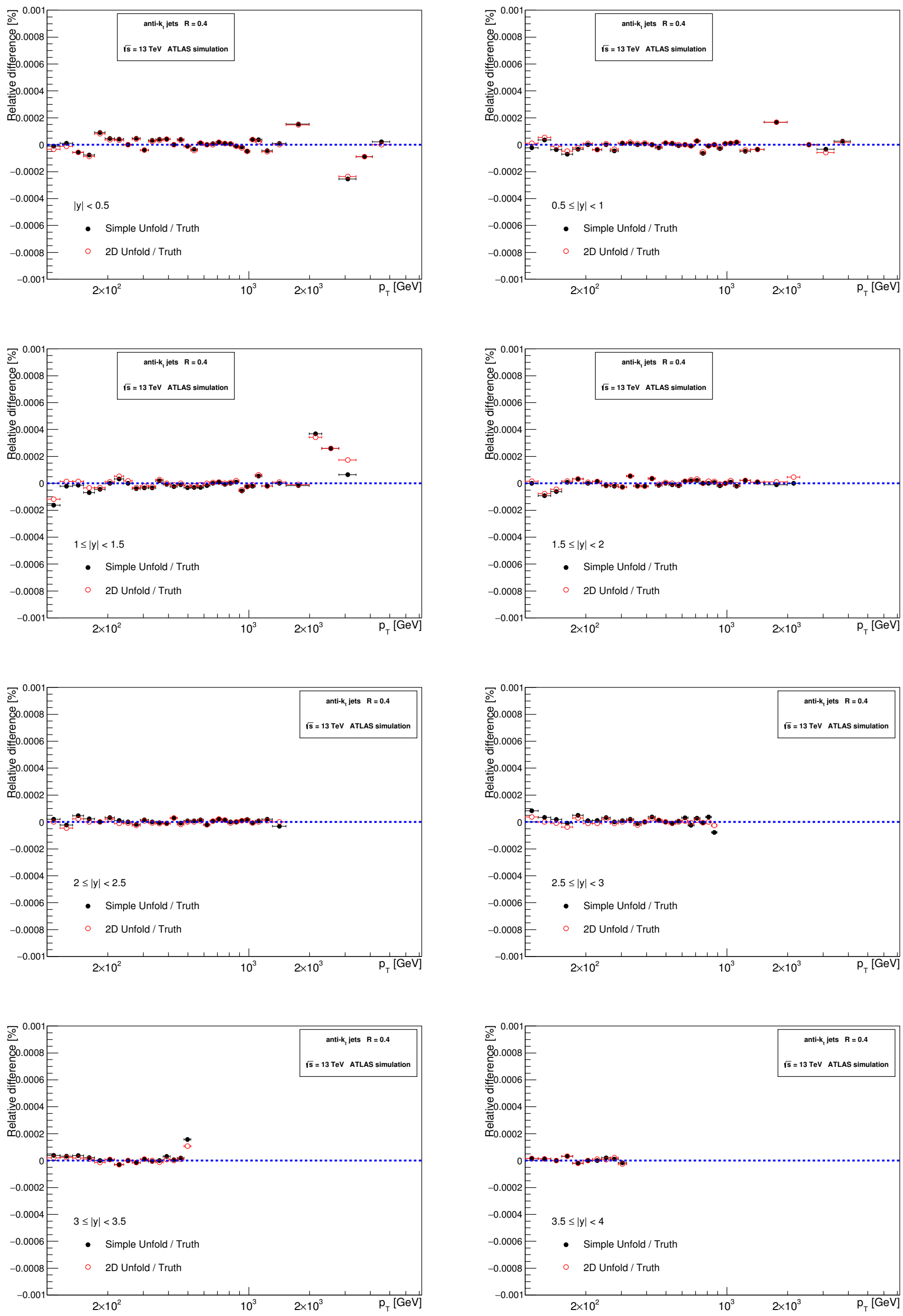

Figure B.5: Comparison of results obtained by two unfolding method - simple and 2D unfolding - with the p_T spectra of truth jets for 8 different rapidity bins.

Appendix C

NLO QCD Prediction

C.1 Predictions for Run I and Run II

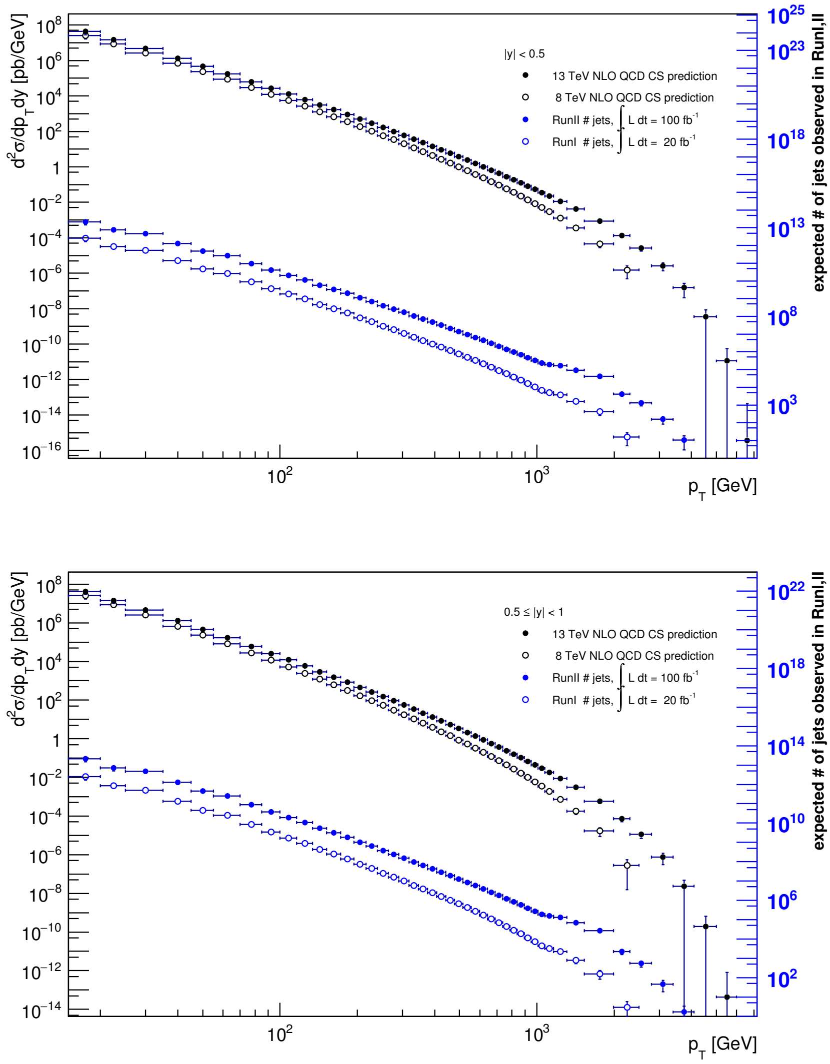

Figure C.1: Comparison of NLO QCD prediction of double differential inclusive jet cross section (black) in p_T and rapidity of pp collisions at $\sqrt{s} = 13\,\text{TeV}$ (filled circles) corresponding to LHC Run II and $\sqrt{s} = 8\,\text{TeV}$ (empty circles) corresponding to LHC Run I. The cross section is multiplied by integrated luminosities and p_T bin width to obtain expected number of jets observed in each p_T bin (blue). Figures show the comparison for $0.5 < |y|$ (top) and $0.5 \leq |y| < 1$ (bottom) rapidity bins.

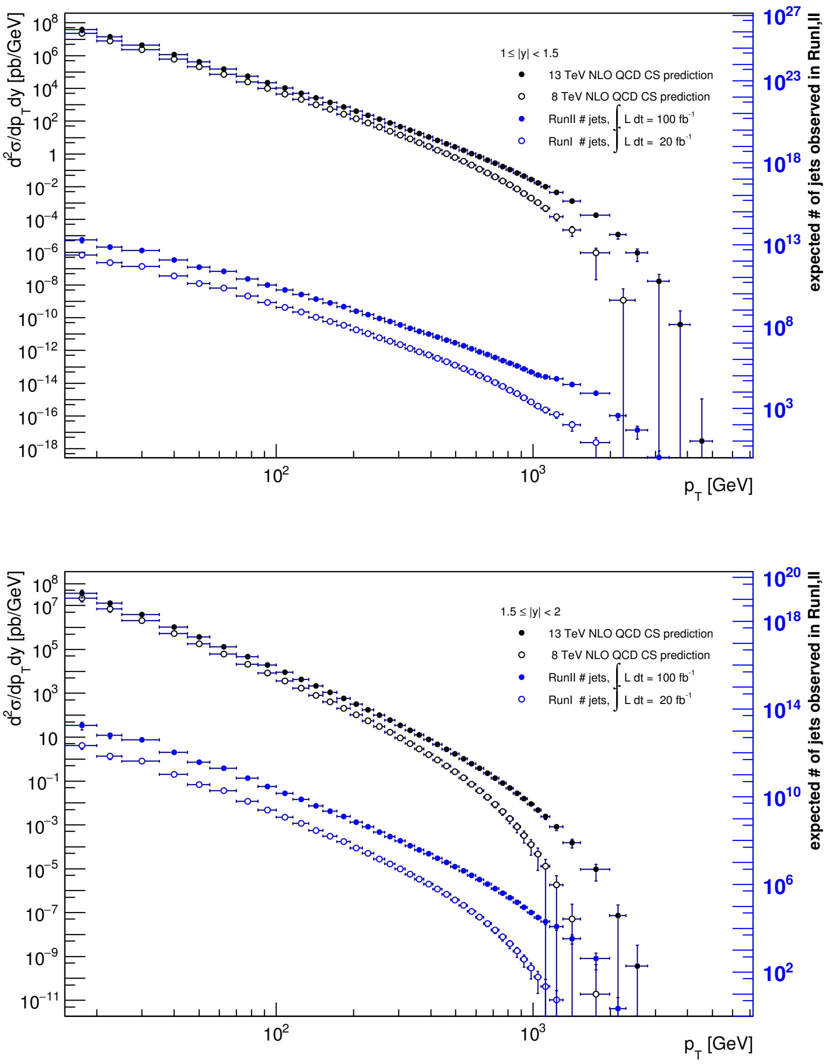

Figure C.2: Comparison of NLO QCD prediction of double differential inclusive jet cross section (black) in p_T and rapidity of pp collisions at $\sqrt{s} = 13$ TeV (filled circles) corresponding to LHC Run II and $\sqrt{s} = 8$ TeV (empty circles) corresponding to LHC Run I. The cross section is multiplied by integrated luminosities and p_T bin width to obtain expected number of jets observed in each p_T bin (blue). Figures show the comparison for $1 \leq |y| < 1.5$ (top) and $1.5 \leq |y| < 2$ (bottom) rapidity bins.

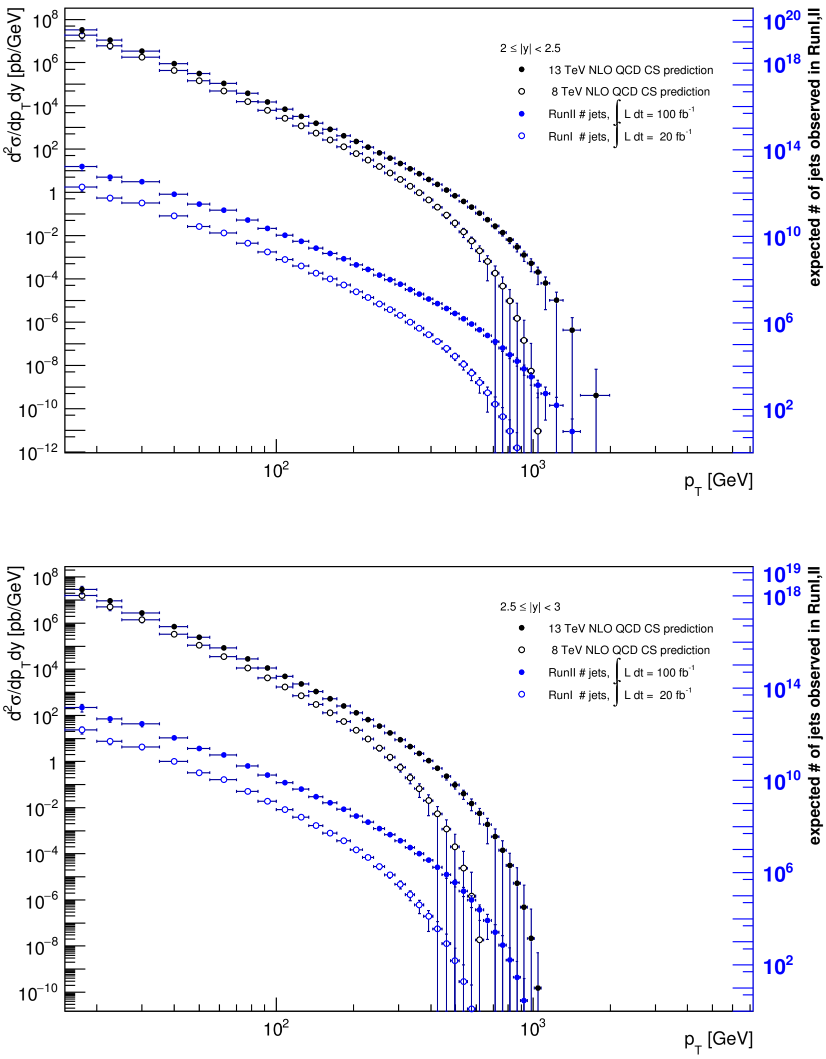

Figure C.3: Comparison of NLO QCD prediction of double differential inclusive jet cross section (black) in p_T and rapidity of pp collisions at $\sqrt{s} = 13$ TeV (filled circles) corresponding to LHC Run II and $\sqrt{s} = 8$ TeV (empty circles) corresponding to LHC Run I. The cross section is multiplied by integrated luminosities and p_T bin width to obtain expected number of jets observed in each p_T bin (blue). Figures show the comparison for $2 \leq |y| < 2.5$ (top) and $2.5 \leq |y| < 3$ (bottom) rapidity bins.

C.2 NLO Uncertainties

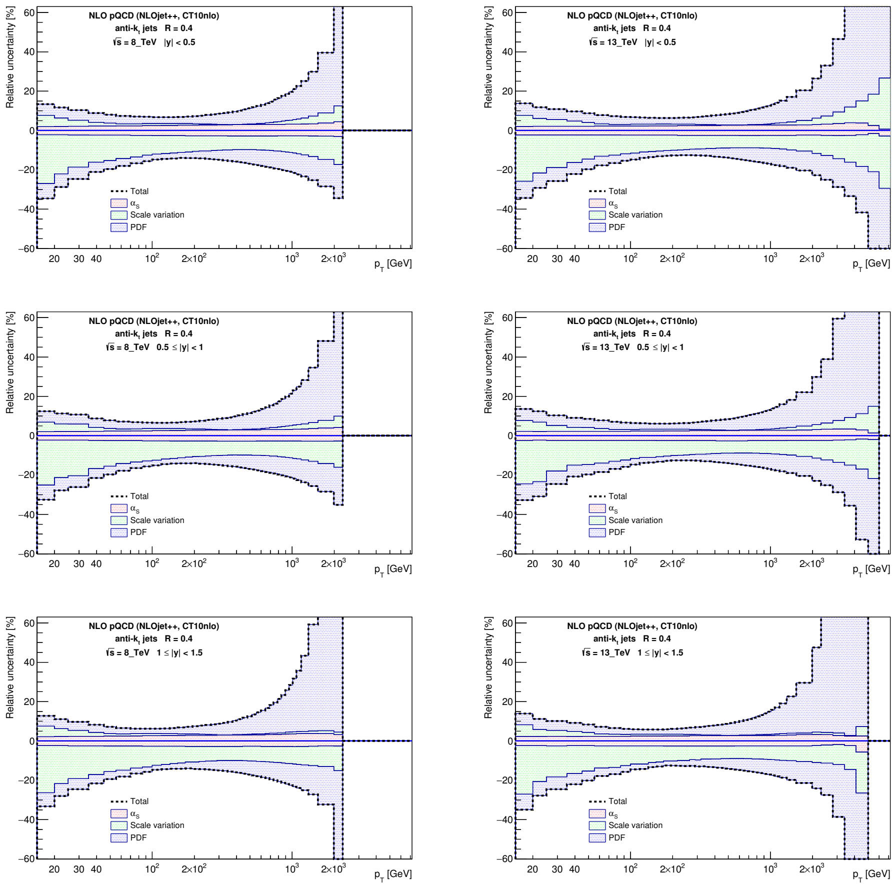

Figure C.4: NLO uncertainties for NLO QCD predictions of inclusive jet double differential cross section of pp collisions at $\sqrt{s} = 8\,\text{TeV}$ (left) and $\sqrt{s} = 13\,\text{TeV}$ (right) for $|y| < 0.5$ (top), $0.5 \leq |y| < 1$ (middle) and $1 \leq |y| < 1.5$ (bottom) rapidity bins.

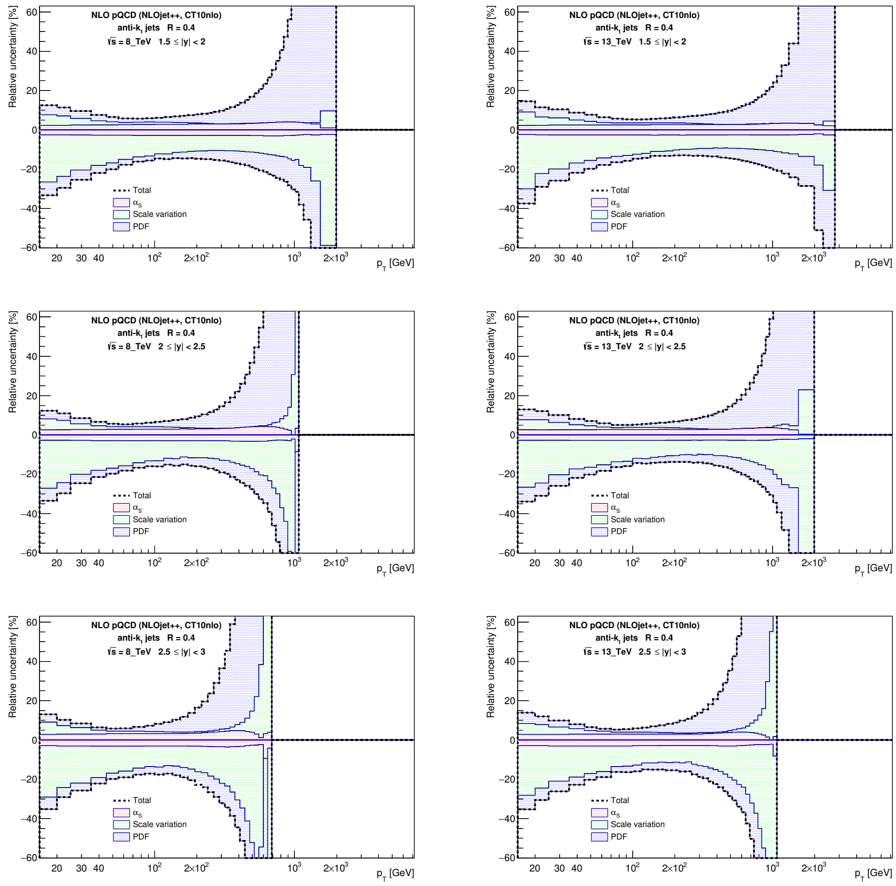

Figure C.5: NLO uncertainties for NLO QCD predictions of inclusive jet double differential cross section of *pp* collisions at $\sqrt{s} = 8\,\text{TeV}$ (left) and $\sqrt{s} = 13\,\text{TeV}$ (right) for $1.5 \leq |y| < 2$ (top), $2 \leq |y| < 2.5$ (middle) and $2.5 \leq |y| < 3$ (bottom) rapidity bins.

C.3 Pythia and NLO

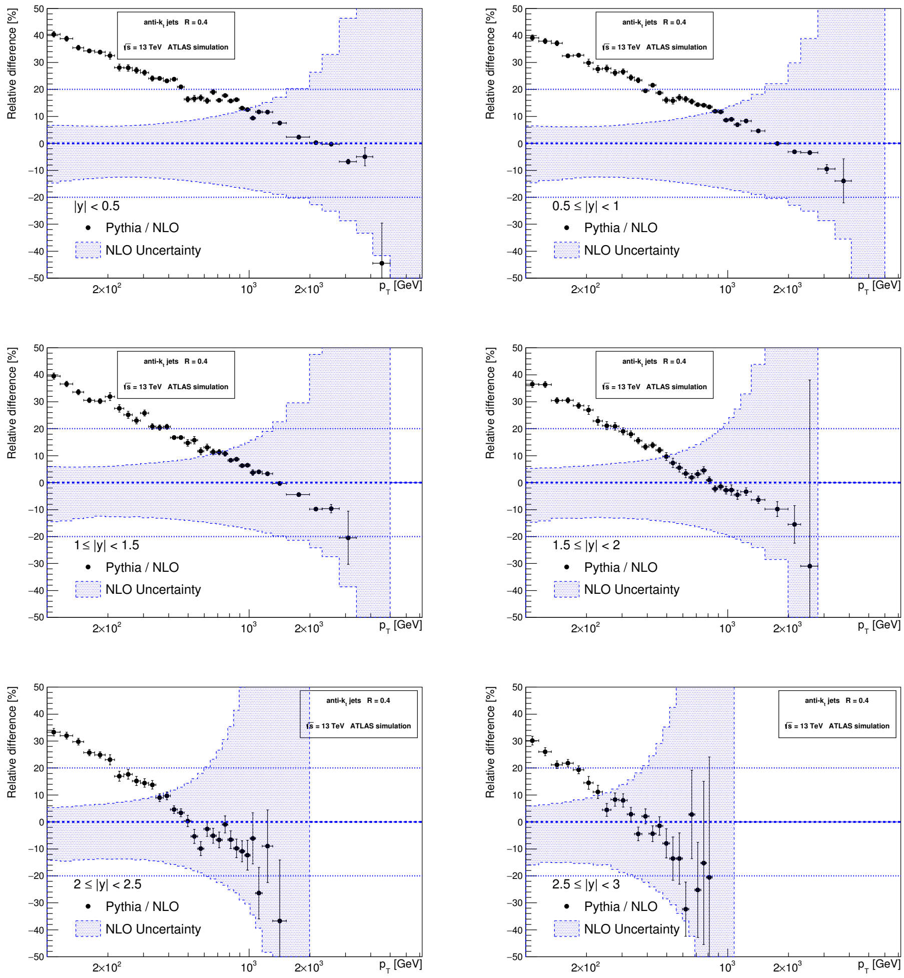

Figure C.6: Comparison of PYTHIA8 prediction with NLO QCD prediction of inclusive jet double differential cross section in p_T and rapidity for six different rapidity bins. Blue area represents the uncertainties of NLO QCD predictions.

Bibliography

[1] S. Durr, "Lattice qcd for pedestrians." http://www.physi.uni-heidelberg.de/Forschung/he/LHCb/documents/WorkshopNeckarzFeb13/durr_neckarzimmern.pdf, 2015. [Online; accessed 16-April-2015].

[2] "Standard model — Wikipedia, the free encyclopedia." http://en.wikipedia.org/wiki/Standard_Model, 2015.

[3] H. Georgi, *Lie Algebras in Particle Physics: From Isospin to Unified Theories*. Frontiers in Physics Series, Westview Press, 1999.

[4] "Eightfold way — Wikipedia, the free encyclopedia." http://de.wikipedia.org/wiki/Eightfold_Way, 2015.

[5] W. Greiner, D. Bromley, S. Schramm, and E. Stein, *Quantum Chromodynamics*. Springer, 2007.

[6] M. Dordevic, "Standard Model physics results from ATLAS and CMS," Tech. Rep. CMS-CR-2014-251, CERN, Geneva, Oct 2014.

[7] "Atlas experiment@2015 cern." http://www.atlas.ch/photos/index.html, 2015.

[8] *Expected performance of the ATLAS experiment: detector, trigger and physics*. Geneva: CERN, 2009.

[9] E. Halkiadakis, "Proceedings for TASI 2009 Summer School on 'Physics of the Large and the Small': Introduction to the LHC experiments," 2010.

[10] B. Isildak, "Measurement of the differential dijet production cross section in proton-proton collisions at $\sqrt{s} = 7$ tev," 2013.

[11] Z. Hubacek, "Measurement of the Three-jet Mass Cross Section in $p\bar{p}$ Collisions at $\sqrt{s} = 1.96$ TeV," 2010.

[12] C. Colaboration, "Observation of top quark production in $\overline{p}p$ collisions with the collider detector at fermilab," *Phys. Rev. Lett.*, vol. 74, pp. 2626–2631, Apr 1995.

[13] D. Colaboration, "Search for high mass top quark production in $p\overline{p}$ collisions at $\sqrt{s} =$ 1.8 tev," *Phys. Rev. Lett.*, vol. 74, pp. 2422–2426, Mar 1995.

[14] G. Aad *et al.*, "Observation of a new particle in the search for the Standard Model Higgs boson with the ATLAS detector at the LHC," *Phys.Lett.*, vol. B716, pp. 1–29, 2012.

[15] "Physics at run 2 the ultimate search engine: Lhc." `http://indico.cern.ch/event/251191/session/0/material/slides/0?contribId=1`, 2015. [Online; accessed 14-April-2015].

[16] K. Olive *et al.*, "Review of Particle Physics," *Chin.Phys.*, vol. C38, p. 090001, 2014.

[17] J. Horejsi, *Fundamentals of Electroweak Theory.* Karolinum Press, 2002.

[18] D. Griffiths, *Introduction to Elementary Particles.* Physics textbook, Wiley, 2008.

[19] W. Cottingham and D. Greenwood, *An Introduction to the Standard Model of Particle Physics.* Cambridge University Press, 2007.

[20] T. Nakano and K. Nishijima, "Charge independence for v-particles," *Progress of Theoretical Physics*, vol. 10, no. 5, pp. 581–582, 1953.

[21] M. Gell-Mann, "The interpretation of the new particles as displaced charge multiplets," *Il Nuovo Cimento*, vol. 4, no. 2, pp. 848–866, 1956.

[22] M. Gell-Mann and Y. Ne'eman, *The eightfold way.* Frontiers in Physics, New York, NY: Benjamin, 1964.

[23] G. Zweig, "An SU_3 model for strong interaction symmetry and its breaking; Version 2," p. 80 p, Feb 1964.

[24] M. Gell-Mann and H. Fritzsch, *Murray Gell-Mann: selected papers.* World Scientific series in 20th century physics, Singapore: World Scientific, 2010.

[25] S. Okubo, "Note on unitary symmetry in strong interactions," *Progress of Theoretical Physics*, vol. 27, no. 5, pp. 949–966, 1962.

[26] S. L. Glashow, J. Iliopoulos, and L. Maiani, "Weak interactions with lepton-hadron symmetry," *Phys. Rev. D*, vol. 2, pp. 1285–1292, Oct 1970.

[27] M. Kobayashi and T. Maskawa, "Cp-violation in the renormalizable theory of weak interaction," *Progress of Theoretical Physics*, vol. 49, no. 2, pp. 652–657, 1973.

[28] E. D. Bloom, D. H. Coward, H. DeStaebler, J. Drees, G. Miller, L. W. Mo, R. E. Taylor, M. Breidenbach, J. I. Friedman, G. C. Hartmann, and H. W. Kendall, "High-energy inelastic $e - p$ scattering at $6°$ and $10°$," *Phys. Rev. Lett.*, vol. 23, pp. 930–934, Oct 1969.

[29] K. Olive *et al.*, "Review of Particle Physics," *Chin.Phys.*, vol. C38, p. 090001, 2014.

[30] C. N. Yang and R. L. Mills, "Conservation of isotopic spin and isotopic gauge invariance," *Phys. Rev.*, vol. 96, pp. 191–195, 1954.

[31] P. W. Higgs, "Broken symmetries and the masses of gauge bosons," *Phys. Rev. Lett.*, vol. 13, pp. 508–509, Oct 1964.

[32] L. Faddeev and V. Popov, "Feynman diagrams for the yang-mills field," *Physics Letters B*, vol. 25, no. 1, pp. 29 – 30, 1967.

[33] D. J. Gross and F. Wilczek, "Ultraviolet behavior of non-abelian gauge theories," *Phys. Rev. Lett.*, vol. 30, pp. 1343–1346, Jun 1973.

[34] "The history of qcd — cern courier." `http://cerncourier.com/cws/article/cern/50796`, 2015.

[35] R. Gupta, "Introduction to lattice QCD: Course," pp. 83–219, 1997.

[36] A. Ukawa, "Kenneth Wilson and lattice QCD," 2015.

[37] L. Evans and P. Bryant, "Lhc machine," *Journal of Instrumentation*, vol. 3, no. 08, p. S08001, 2008.

[38] G. Landsberg, "LHC: Past, Present, and Future," 2013.

[39] R. Bruce, G. Arduini, S. Fartoukh, M. Giovannozzi, M. Lamont, *et al.*, "Baseline LHC machine parameters and configuration of the 2015 proton run," 2014.

[40] "Future prospects for higgs measurements at lhc run 2+3." `http://www.nikhef.nl/pub/BND2014/projects/ILC-vs-LHC-HL/LHC_Aspen_2014_Kroha.pdf`, 2014.

[41] T. A. Collaboration, "The atlas experiment at the cern large hadron collider," *Journal of Instrumentation*, vol. 3, no. 08, p. S08003, 2008.

[42] T. D. Lee and M. Nauenberg, "Degenerate systems and mass singularities," *Phys. Rev.*, vol. 133, pp. B1549–B1562, Mar 1964.

[43] T. Kinoshita, "Mass singularities of feynman amplitudes," *Journal of Mathematical Physics*, vol. 3, no. 4, 1962.

[44] G. Aad *et al.*, "Expected Performance of the ATLAS Experiment - Detector, Trigger and Physics," 2009.

[45] G. C. Blazey, J. R. Dittmann, S. D. Ellis, V. D. Elvira, K. Frame, *et al.*, "Run II jet physics," pp. 47–77, 2000.

[46] M. Cacciari, G. P. Salam, and G. Soyez, "The Anti-k(t) jet clustering algorithm," *JHEP*, vol. 0804, p. 063, 2008.

[47] T. Sjostrand, S. Mrenna, and P. Z. Skands, "A Brief Introduction to PYTHIA 8.1," *Comput.Phys.Commun.*, vol. 178, pp. 852–867, 2008.

[48] S. Agostinelli *et al.*, "GEANT4: A Simulation toolkit," *Nucl.Instrum.Meth.*, vol. A506, pp. 250–303, 2003.

[49] W. Lukas, "Fast Simulation for ATLAS: Atlfast-II and ISF," 2012.

[50] J. Bossio, "Applyjetcalibration2014." `https://twiki.cern.ch/twiki/bin/viewauth/AtlasProtected/ApplyJetCalibration2014`, 2015. [Online; accessed 16-April-2015].

[51] V. Blobel, "Unfolding methods in high-energy physics experiments," p. 40 p, Dec 1984.

[52] G. D'Agostini, "Improved iterative Bayesian unfolding," *Phys.Rev.*, p. 31, 2010.

[53] A. Hocker and V. Kartvelishvili, "SVD approach to data unfolding," *Nucl.Instrum.Meth.*, vol. A372, pp. 469–481, 1996.

[54] B. Malaescu, "An Iterative, Dynamically Stabilized(IDS) Method of Data Unfolding," 2011.

[55] H.-L. Lai, M. Guzzi, J. Huston, Z. Li, P. M. Nadolsky, *et al.*, "New parton distributions for collider physics," *Phys.Rev.*, vol. D82, p. 074024, 2010.

[56] S. Wahrmund, "Atlas tunes for mpi." `http://indico.cern.ch/event/184925/session/4/contribution/19/material/slides/0.pdf`, 2015. [Online; accessed 16-April-2015].

[57] T. Carli, E. Ertel, E. Fullana Torregrosa, A. Hrynevich, Z. Hubacek, B. Malaescu, N. Meric, C. Meyer, V. Pleskot, S. Shimizu, P. Starovoitov, G. Vardanyan, and S. Yanush, "Measurement of inclusive jet production in pp collisions at $\sqrt{s} = 7$ TeV using the ATLAS detector (Supporting Documentation)," Tech. Rep. ATL-COM-PHYS-2013-1390, CERN, Geneva, Oct 2013.

[58] Z. Nagy, "Next-to-leading order calculation of three jet observables in hadron hadron collision," *Phys.Rev.*, vol. D68, p. 094002, 2003.